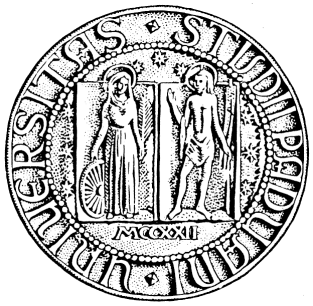

Università degli Studi di Padova
DIPARTIMENTO DI INGEGNERIA INDUSTRIALE
Corso di Laurea Magistrale in Ingegneria Aerospaziale

Tesi di Laurea Magistrale

Aerodynamic Analysis and Design of a Transonic Fan with Clean and Distortion Inflow using Multi-Fidelity Methods

Laureando:
Alessandro Visentin

Relatore:
Prof. Ernesto Benini

Correlatori:
Ing. Luca Menegozzo
Ing. Andrea Magrini

Anno accademico 2020 / 2021

Università degli Studi di Padova
Dipartimento di Ingegneria Industriale
Via Venezia 1, 35131 — Padova

Feel the fear and do it anyway!
Susan Jeffers

Un ringraziamento speciale va alla mia famiglia, che mi ha sempre supportato durante questo lungo percorso.

Grazie agli amici di università e non, per la loro presenza e per avermi regalato momenti di spensieratezza e tante risate.

Ringrazio inoltre il Prof. Benini, per avermi dato la possibilità di collaborare con il gruppo di ricerca COMETES e gli Ingg. Luca Menegozzo ed Andrea Magrini, per la loro disponibilità e le conoscenze trasferitemi.

Abstract

The following dissertation focuses on a methodology for the analysis and preliminary design of axial compressors operating under clean and distortion inflow conditions.

Non-uniform operating conditions inherently characterize BLI aircraft concepts, recently devised to be a way to make air flights more sustainable. Chapter 1 offers an overview about this topic, besides illustrating some recent research contributions and clarifying the objectives of the thesis. In this regard, the main goal is the development and testing of a low-order numerical approach, suitable to be used within an optimization loop, and the assessment of the results through higher-fidelity calculations, in order to introduce further strides in the design optimization, even combining the two tools in an iterative process.

Chapter 2 is the cornerstone of the work and describes the methodology adopted. The numerical analysis is performed by SATURN, a software developed within the COMETES research group and based on a 1D Mean-Line (ML) solver. It enables a quasi-2D discretization in order to deal also with non-uniform boundary conditions (BCs) at the inlet, which can be derived from arbitrary 2D distributions. In this study BCs are derived from a full-annulus CFD model. NASA R4 transonic fan rotor is the test case considered and, at first, its predicted performance under clean conditions is validated through the use of experimental data. After that, the Discretized Compressor (DC) approach is presented and a sensitivity analysis is conducted. Then, the design procedure is discussed and the combination between SATURN and NOPTURN, a Matlab optimizer based on genetic algorithms, is described. The latter aims to modify the blade geometry to optimize some performance objectives and to fulfil the imposed constraints. The successive step is also realized in Matlab and consists in the 3D geometry reconstruction for the import in ANSYS-CFX. Here, single-passage or full-annulus domains are provided for the CFD calculation, respectively, under uniform or distorted inflow conditions. Several single-passage RANS simulations are launched in the first case, whereas the full-annulus analysis is planned. The chapter ends describing the novel procedure introduced to extract the boundary conditions from full-annulus CFD results, according to the inlet discretization required by the ML tool.

Chapter 3 provides the performance obtained from the analysis and design investigations. The analysis under distorted configuration and the design under clean conditions present a comparison between the ML results and CFD outputs, used as benchmark when experimental data are not available. Meanwhile, the design under distortion reports only ML results for baseline and optimized geometry.

The conclusions recall the achieved objectives and propose further developments.

Abstract

La seguente tesi affronta una metodologia per l'analisi ed il design preliminare di compressori assiali in condizioni di flusso uniforme e distorto all'ingresso.

Condizioni operative non uniformi sono la caratteristica principale dei motori aeronautici di tipo BLI, recentemente progettati per ridurre l'impatto ambientale. Il capitolo 1 offre una panoramica su questo argomento, oltre ad illustrare una serie di contributi scientifici sul tema e ad indicare gli obiettivi dell'elaborato. A tal riguardo, lo scopo principale consiste nell'utilizzo di un metodo numerico di basso-livello, adatto per essere utilizzato in un processo di ottimizzazione e nella valutazione dei risultati ottenuti, tramite calcoli più affidabili condotti per mezzo della CFD. Si auspica che le conclusioni tratte possano aprire la strada ad ulteriori sviluppi nel *design optimization*, come la combinazione dei due metodi all'interno di un processo iterativo.

Il capitolo 2 rappresenta il cuore della tesi e descrive la metodologia adottata. L'analisi numerica è realizzata tramite SATURN, un software sviluppato all'interno del gruppo di ricerca COMETES e basato su un solutore *Mean-Line* (ML) monodimensionale. Questo permette una discretizzazione quasi-2D, in modo da poter considerare anche condizioni all'ingresso (BCs) non uniformi, le quali possono derivare da una qualsiasi distribuzione 2D. Nel presente studio tali BCs provengono da un modello CFD *full-annulus*. Il rotore di fan transonico NASA R4 è impiegato come caso di prova e le sue performance, predette dal ML nel caso pulito, sono inizialmente validate tramite il confronto con dati sperimentali. In seguito, viene introdotto l'approccio *Discretized Compressor* (DC) ed è condotta un'analisi di sensibilità. Successivamente viene presentata la procedura di *design*, che si fonda sulla combinazione tra SATURN e NOPTURN, un codice di ottimizzazione scritto in Matlab e basato su algoritmi genetici. Quest'ultimo mira a modificare la geometria della pala, al fine di massimizzare le performance desiderate, rispettando i vincoli imposti. Il passo successivo avviene sempre in Matlab e consiste nella ricostruzione 3D della geometria per l'importazione in ANSYS-CFX. Qui, domini *single-passage* o *full-annulus* sono forniti per i calcoli della CFD, rispettivamente in condizioni di flusso pulito o distorto. Diverse simulazioni RANS sono lanciate nel primo caso, mentre l'analisi *full-annulus* è definita per la sua realizzazione in lavori futuri. Il capitolo termina descrivendo la procedura utilizzata per estrarre le condizioni al contorno dai risultati della CFD, secondo la discretizzazione richiesta dal codice ML.

Il capitolo 3 fornisce le performance ottenute dalle analisi e design. L'analisi in condizioni distorte ed il design in condizioni pulite riportano il confronto tra i risultati del ML e della CFD, considerando quest'ultima come riferimento in assenza di dati sperimentali. Invece, per quanto riguarda il design in condizioni distorte, vengono riportate le performance predette dal ML con la geometria originale ed ottimizzata.

Le conclusioni richiamano gli obiettivi e presentano possibili sviluppi futuri.

Contents

Nomenclature

A	[m^2]	Area
c	[m]	Chord
c_p	[J/kgK]	Specific heat
CM	[−]	Choking Margin
e	[−]	Relative error
F	[−]	Fitness
F_x	[N]	Net streamwise force
h	[J/kg]	Specific enthalpy
j	[−]	Index
K	[−]	Coefficient
k	[−]	Heat capacity ratio
M	[−]	Mach number
$\dot{m}$	[kg/s]	Mass flow
$\dot{m}_c$	[kg/s]	Corrected mass flow
$\dot{m}_{PE}$	[kg/s]	Clean $\dot{m}_c$ at peak efficiency
N	[−]	Number
N_r	[−]	Number of spanwise sections
N_θ	[−]	Number of circumferential sectors
P	[−]	Penalty
p	[Pa]	Pressure
P_k	[W]	Net mechanical flow power
P_v	[W]	Volumetric flow power
PSC	[−]	Power Saving Coefficient
R	[J/kgK]	Gas constant
R_e	[−]	Reynolds number
r	[m]	Radial coordinate
r_c	[m]	Curvature radius
SM	[−]	Stall Margin
T	[K]	Temperature
t	[m]	Thickness
TPR	[−]	Total Pressure Ratio
TTR	[−]	Total Temperature Ratio
u	[m/s]	Blade velocity
v	[m/s]	Flow velocity
V_∞	[m/s]	Freestream speed
x	[−]	Optimization variable
z	[m]	Axial coordinate

Greek

α	[°]	Flow angle
β	[°]	Blade angle
δ	[°]	Flow deviation angle
η_{iso}	[−]	Isentropic efficiency
θ	[°]	Circumferential coordinate
μ	[Pa/s]	Dynamic viscosity
ξ	[−]	Blockage factor
ρ	[kg/m^3]	Density
σ_x	[−]	Variance along x-axis
σ_y	[−]	Variance along y-axis
Φ	[W]	Viscous dissipation
ϕ	[−]	Generic variable
φ	[−]	Relaxation factor
ω	[rad/s]	Angular velocity

Subscripts

0	Total flow quantity
1	Inlet plane
2	Outlet plane
b	Blade
$base$	Baseline geometry
con	Constraint
des	Design
gen	Generation
ind	Individual
∞	Over the entire volume
n	Iteration number
obj	Objective
ref	Reference value
rel	Relative flow quantity
$surf$	Related to boundary layer
shr	Shroud
tip	Tip clearance losses

Acronyms

AIP	Aerodynamic Interface Plane
BC	Boundary Condition
BLI	Boundary Layer Ingestion
CFD	Computational Fluid Dynamics
DC	Discretized Compressor
DC_{60}	Distortion Coefficient
DFC	Distributed Fans Concept
DNS	Direct Numerical Simulations
EA	Evolutionary Algorithm
EGV	Exit Guide Vane
EU	European Union
GA	Genetic Algorithm
GEAE	General Electric Aircraft Engines
GGI	General Grid Interface
GHG	Green-House Gases
ICAO	International Civil Aviation Organization
IGV	Inlet Guide Vane
LE	Leading Edge
LES	Large Eddy Simulations
ML	Mean-Line
MOOP	Multi-Objective Optimization Problem
NOPTURN	Numerical OPtimization of TURbofaN
OGV	Outlet Guide Vane
PFC	Propulsive Fuselage Concept
PS	Pressure Side
RANS	Reynolds-Averaged Navier-Stokes
REC	Rear Engines Concept
RF	Radiative Forcing
RMS	Root Mean Square
RPK	Revenue Passenger Kilometre
SATURN	Systematic Analysis of TURbofaN
SS	Suction Side
SST	Shear Stress Transport
TE	Trailing Edge
TeDP	Turbo-electric Distributed Propulsion
URANS	Unsteady RANS

List of Figures

List of Tables

Chapter 1

Introduction

A brief overview on the current aviation challenges is illustrated and a novel engine concept, predicted to be one of the possible solutions to enhance flight sustainability, is presented. After that, a literature review describes how this new concept has been investigated by other authors. The objectives of the thesis are finally introduced.

1.1 Overview

The general context in which the following dissertation is inserted concerns the aviation and climate change, challenges and solutions.

Nowadays anthropogenic climate change is widely accepted amongst the scientific community and, during the years, significant global efforts have been made to comprehend its origin, studying the physics and chemistry of the atmosphere, and focusing on how to reduce its impact on the environment. The last international treaty on climate change was the Paris Agreement, stipulated on 12 December 2015. The principal goal is to limit global warming to well below 2, preferably to 1.5 degrees Celsius, compared to pre-industrial levels.

In this challenge the aviation industry plays a role as well. Figure 1.1 clearly shows the impact of certain gas emissions, and human being has contributed to modify their natural balance. Different metrics exist to evaluate the emissions effects on the atmosphere, but the commonly used is Radiative Forcing (RF). To clarify, this is a measure of the perturbation of the Earth-atmosphere energy budget since 1750, by convention in Intergovernmental Panel on Climate Change (IPCC) usage, resulting from changes in trace gases and particles in the atmosphere and other effects such as albedo, and is measured in units of watts per square metre (Wm^{-2}) at the top of the atmosphere [1]. The RF components from aviation arise from the following processes:

1. emission of CO_2 (positive RF);
2. emission of NO_x (positive RF). This term is the sum of three component terms: production of tropospheric O_3 (positive RF); a longer-term reduction in ambient methane (CH_4) (negative RF); a further longer-term small decrease in O_3 (negative RF);
3. emission of H_2O (positive RF);

4. formation of persistent linear contrails (positive RF);
5. aviation-induced cloudiness (positive RF);
6. emission of sulphate particles (negative RF);
7. emission of soot particles (positive RF).

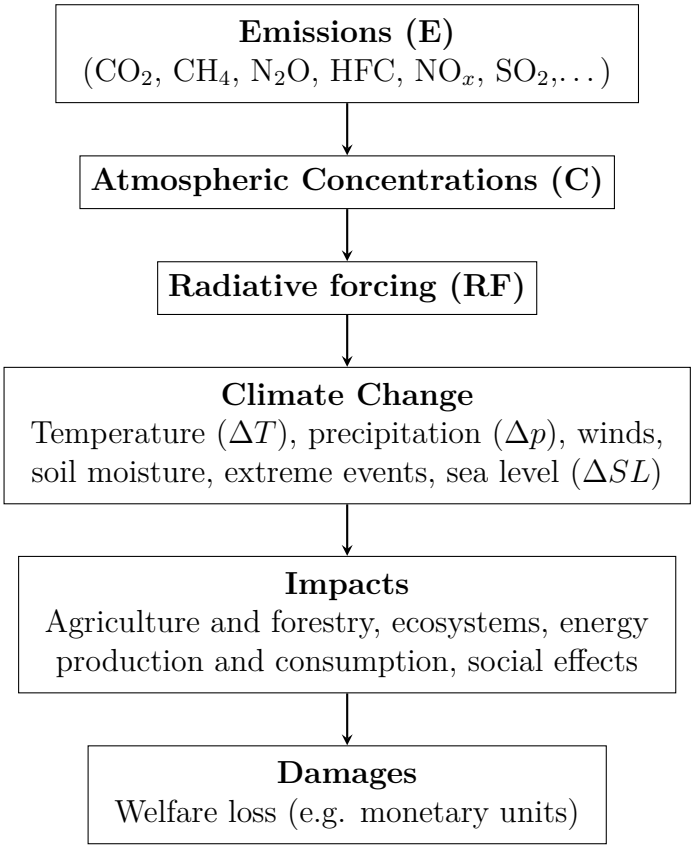

Figure 1.1: *Cause and effect chain of the potential climate effect of emissions. [2]*

The Kyoto Protocol, defined in a conference in 1997 and promoted to law in 2005, is the first international agreement on management and reduction of GreenHouse Gases (GHG) emissions. However, in this occasion the international aviation emissions were excluded, as they were considered negligible compared to other sectors. The responsibility to introduce some emissions limitations was given to the International Civil Aviation Organization (ICAO). Because of the slow decisional process, Europe moved the first steps towards the inclusion of the aviation emissions in its trading scheme from 2012. Even if only CO_2 was considered, being the dominant component of aircraft emissions, this was an important signal to mobilize ICAO to take into account the matter and introduce global actions [3]. In fact, aviation was recognized as the world's fastest growing source of GHG, despite a relevant improvement in efficiency of aircraft and flight operations. The reason is the steady growth of air travel since the first transatlantic flight in 1927 and the projection to maintain a close to 5% growth for the next years [4]. For instance, from 2013 to 2018, annual global growth rates of Revenue Passenger Kilometres (RPKs, one passenger

travelling one kilometre is one RPK) ranged from 5.7 to 7.4 percent [5]. Globally, aviation produced 2.4% of total CO_2 emissions in 2018 and the total contribution of commercial aviation is approximately 5 percent of the world's climate-warming problem. Anyway, the interest in mitigation of aviation climate forcing continues to grow and different actions have been planned. They involve improvements in air traffic management and operational practises, the usage of alternative fuels to kerosene, the change of cruise altitudes in order to reduce the non-CO_2 effects, the reduction of weight through material changes, aerodynamic improvements, but above all the enhancement of fuel efficiency. This latter has been the major area of research and development for many decades and is the principal aspect addressed in this work.

More in detail, the novelty of the thesis stands in the design procedure for axial compressors or fans, focusing on new concept of air civil turbofan engines, devised to improve the fuel efficiency of air transport. Such new class of aircraft is known to incorporate a Boundary Layer Ingestion (BLI) propulsive system, that is described more deeply in the next subsection.

1.1.1 BLI system

The BLI propulsive system is a relatively new engine idea, developed to give a contribution to more sustainable propulsion frames, as requested by the increasingly stringent environmental regulations. Recently, different novel concepts have been devised, characterized by engines embedded in the aircraft fuselage. As a result, part of the air inflow consists of the low-speed boundary layer created over the external surface.

Numerous EU and NASA research projects defined several aircraft layouts, that can be grouped into three principal categories: Propulsive Fuselage Concept (PFC), Rear Engines Concept (REC) and Distributed Fans Concept (DFC). In the first, a conventional airplane layout is present with the addition of a nacelle positioned at the tail-cone of the fuselage, ingesting the wake of the aft aircraft body. The incoming boundary layer is therefore concentric and the propulsor deals with a radially-dominant distortion (360°). The system can be either mechanically or electrically driven. An existing configuration is offered by CENTRELINE, reported in Figure 1.2a, a project funded by the European Union as part of Horizon 2020 Framework Programme. The second category moves the underwing podded engines to the rear fuselage, with no turbo-electric propulsion. One potential engine layout is displayed in Figure 1.2b and comes from the study conducted on D8 transport aircraft [6], according to N+3 NASA program. DFC is the most challenging configuration, due to its tricky fuselage-engine integration. The fuselage presents blended-wing and hybrid wing body shapes, and multiple propulsors, embedded in a continuous nacelle, are responsible for thrust generation. Figure 1.2c represents the solution proposed by N3-X research project by NASA. Here, a Turbo-electric Distributed Propulsion (TeDP) system is employed. The multiple fans work exploiting the electrical power generated by two wingtip-mounted turbofan engines. In the last two engine families, the incoming flow is mainly affected by circumferential distortion

(180°), in contrast to PFC.

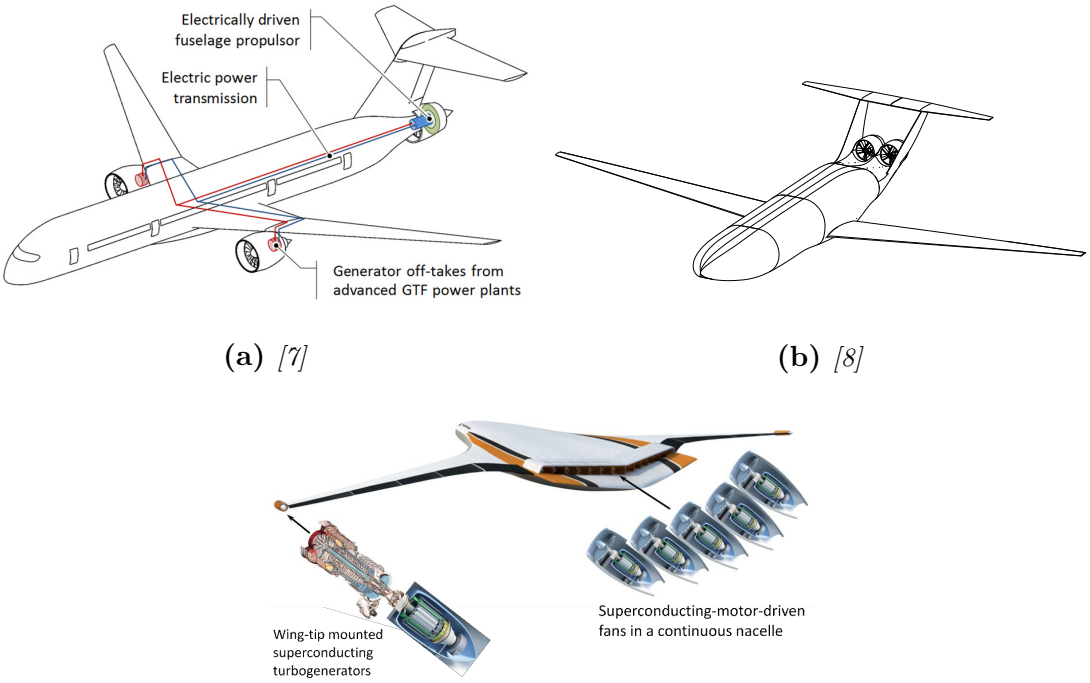

(a) *[7]* **(b)** *[8]*

(c) *[9]*

Figure 1.2: *Layout examples of the three principal BLI concepts.*

Considering all these configurations, BLI system presents some advantages and drawbacks, as well explained in [10].

Pros

- The wake filling process, described later, allows reducing the required power and as consequence reducing fuel burn and emissions;
- Drag is reduced by means of the engine-fuselage integration. In fact, the wetted area decreases;
- The separation between power and thrust generation devices opens to high achievable by-pass ratios;
- The propulsion system is partially or completely shielded by the airframe, thus yielding to a potential noise reduction;
- TeDP implementation, despite the need of superconductivity and cryogenic fuels, represents a disruptive technology that has the potential to produce significant environmental benefits.

Cons

- The engine operates under non-uniform inflow conditions, that affect the performance, introducing internal losses and a premature surge condition;
- Structural fatigue issues can rise from unconventional engine installations;

- Propulsive efficiency is further reduced by a lower total inlet pressure recovery;
- TeDP application increases the overall weight and introduces additional risks due to high-power electrical devices.

The wake filling process, listed among the benefits, is of particular relevance and deserves a deeper description. This aerodynamic phenomenon is the principal reason of fuel efficiency increase. To introduce it, a premise is necessary. In the BLI configuration, the definition of thrust and drag becomes ambiguous due to the engine integration with the airframe. Therefore, the fuel efficiency increase is explained through an approach based on the power balance framework [6, 11]. During this mechanical energy analysis, a control volume is defined with inner boundary covering the body surface and outer boundary at infinity to simplify the problem. The unit vector $\hat{n}$ points outside the volume, hence into the the aircraft body. The integral mechanical power balance equation is applied over the entire control volume and is obtained instantaneously in steady flows or as a periodic-average in unsteady periodic flow. The formula used is the following:

$$F_x V_\infty = \Phi_\infty - P_k - P_v \tag{1.1}$$

where F_x is the net streamwise force on the body (drag minus thrust) and V_∞ is the freestream speed. P_k is the net mechanical flow power, passing through the propulsor inlet and exit, while P_v is the volumetric flow power, provided by the fluid expanding against atmospheric pressure and negligible for low-speed flows. The volumetric viscous dissipation is represented by Φ_∞ and is the sum of different sources, as shown in Figure 1.3:

$$\Phi_\infty = \Phi_{surf} + \Phi_{wake} + \Phi_{jet} + \Phi_{vortex} \tag{1.2}$$

The first two terms, losses in the boundary layers and in the wakes, represent the usual drag power, while Φ_{vortex} is an unchanged term from non-BLI to BLI systems. The benefit in question concerns the reduction of the dissipation in the jet and wake. Basically, the propulsor re-energizes the wake reducing the wasted kinetic energy. Hence, the power P_k required to produce a given net streamwise force is reduced. A way to quantify this advantage is the Power Saving Coefficient (PSC), expressed as function of the mechanical flow power:

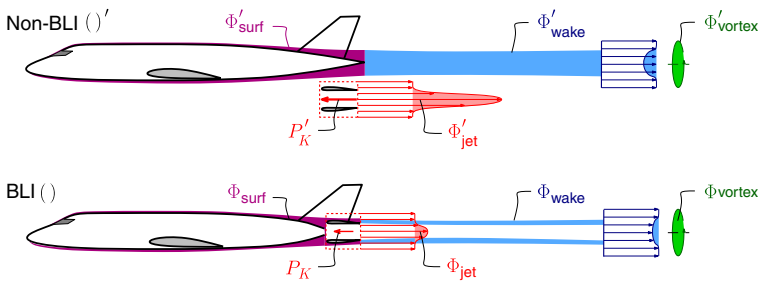

Figure 1.3: *Illustration of power balance terms for boundary layer ingesting (bottom) and conventional (top) aircraft. [6]*

$$\mathrm{PSC} = \frac{P_k' - P_k}{P_k'} = 1 - \frac{P_k}{P_k'} \tag{1.3}$$

However, this approach does not consider the impact of the non-uniform air inflow on the fan component and within the engine, since it is a separate aspect. This latter represents the major drawback because it may offset the aforementioned benefit, introducing internal losses.

1.2 Literature review

Inlet flow distortion has long been recognized to have an impact on fan performance and a significant amount of research effort has been devoted to understand the flow physics and develop multi-fidelity tools to tackle the problem. Here, some research contributions are reported and briefly described.

Lee et al. [12] carry out a conceptual design of a tail-cone thruster system under axisymmetric non-uniform inflow. This PFC layout is one of the first NASA's concepts of the next generation aircraft, named STARC-ABL. Thus, the incoming boundary layer is concentric. The authors focus on the radial distortion at the fan face, given the low circumferential distortion, and use a multi-fidelity design approach. Three iterative steps are followed: a quasi-2D through-flow model to design the fan/EGV, a 3D Reynolds-Averaged Navier-Stokes (RANS) simulation to consider the inlet/fan and the EGV/nozzle interaction and a 3D RANS simulation of the fuselage with the propulsor embedded.

Researches on how to improve the performance of recent BLI engine concepts are also found in literature. For instance, Valencia et al. [13] propose a novel fan configuration for distributed propulsion systems with BLI on an hybrid wing body airframe. The purpose is to re-energize the boundary layer in an alternative way and to perform properly under distorted flow field. A streamline method, based on semi-empirical relations and fan design, is adopted to assess its benefits and to make proposals for further refinements.

An interesting study is conducted by Thollet et al. [14] about the body-force modelling for aerodynamic analysis, extensively discussed in the literature. It is not referred specifically to a distortion case, but the intention is to further extend it to any operating conditions and to non-axisymmetric cases. It represents an alternative way to investigate the air intake-fan interactions and a less prohibitive mode with respect to the cost and complexity of Computational Fluid Dynamics (CFD). The method aims to replace the blades, using a body-force field that produces the same flow features. Two approaches are compared: the field can be generated by an analytical model or the body forces can be extracted directly from a RANS computation. The technique is applied on an air intake test case and the results compared to that obtained with full-annulus unsteady simulations. Moreover, the effect of the blockage term (see section 2.1) is determined.

A body-force modelling approach is also employed in [15] to study a low-speed

cooling fan with inflow distortion. The results are compared to full-annulus Unsteady Reynolds-Averaged Navier-Stokes (URANS) outputs and experimental data, showing a good agreement with the former and some discrepancies with the latter. The research demonstrates the possibility to employ such a method for the first design loops, when the required accuracy is not too challenging.

Cui et al. [16] propose a mixed-fidelity computational fluid dynamics method to study the fan-distortion interaction. The use of high computational techniques, such as DNS and LES, to resolve the entire fan yields accurate results, but are tremendously costly and infeasible within industry. For this reason, the authors decide to model the turbulence, associated with separation, with LES, since the limitations of steady and unsteady RANS for distortion cases, and model the fan geometry with the low-order model IBMSG (known as *blade body-force approach*), modified for unsteady flow calculations and distortion problems. The research is divided into two parts. The first involves the validation of the model through a comparison with the experiment on the Darmstadt Rotor. After that, they focus on the factors that affect the reduction of inlet distortion, such as the fan location and the distortion degree.

Many researchers, before providing a method to face the problem and find a way to design a fan/compressor under distorted conditions, began conducting experimental investigations. Gunn et al. [17] perform high-resolution, full-annulus experimental measurements on a low-speed fan stage operating with a continuous 60 degrees inlet stagnation pressure distortion. The study aims to understand better the 3D flow features and assess the loss generation within the fan due to this non-uniform conditions. The off-design incidence values at Leading Edge (LE) and the associated flow separations are considered the main causes. This research is also realized to be a benchmark for future works on improving the efficiency in BLI fan systems.

In [18] Zhang et al. centre their attention on the inlet distortion effects on the fan aerodynamic stability, with NASA Rotor 67 as test case. Accurate 3D URANS simulations are carried out to achieve the two main goals of the paper, which are the investigation of the influence of CFD time discretization and the fan rotational speed on the stalled operating point and the Stall Margin (SM). The latter is defined as:

$$\mathrm{SM} = \left[\frac{\mathrm{TPR}_{surge}}{\mathrm{TPR}_{ref}} \cdot \frac{\dot{m}_{c,ref}}{\dot{m}_{c,surge}} - 1 \right] \cdot 100\% \tag{1.4}$$

where TPR_{surge} and TPR_{ref} are, respectively, the total pressure ratio near the surge point and at the reference point, typically equal to the peak efficiency condition, whereas $\dot{m}_c$ indicates the corrected mass flow. One of the research conclusions is that SM and SM loss, that is the difference of stall margins between the clean flow case and the distorted case, decrease as the rotational speed decreases.

Fidalgo et al. [19] study the fan-distortion interaction within the aforementioned test case. They examine a 120 degrees distortion of the inlet flow field and run accurate unsteady full-annulus CFD simulations to analyse the entire fan assembly. The intention is to understand how the fan operates at different locations around the annulus and observe the exit flow field as well to make conclusions on the flow mechanism through the fan. A good agreement with respect to the experimental

results is found. Moreover, the researchers introduce a novel post-processing method to extract the fan performance, based on gate functions [20].

Another low-order method has been used since the 1960s to evaluate the impact of inlet distortion. It is called *parallel compressor* and is designed for the analysis of circumferential distortion effects. Cousins et al. [21] research on this field and describe the model concepts, theory and limitations. The initial idea is to treat the compression system under distortion as two isolated compressors operating in parallel under clean conditions with different inlet total pressures, but with the same exit static pressure. One of the drawbacks is that the model applicability is limited to circumferential distortion patterns. Different extensions of the basic model have been presented and utilized over the years to provide a useful tool for the analysis of complex distortion problems as well.

Da et al. [22] offer an overview of the potential of sweep design process on a transonic axial-flow compressor to achieve high aerodynamic performance under distorted inflow conditions.

1.3 Objectives

The present dissertation aims to define a numerical methodology for the analysis and preliminary design of a transonic fan rotor under clean and distortion inflows. NASA/GEAE R4 is considered as test case. In the first part the fan is examined under uniform inlet flow field, while in the second the performance under distorted conditions is assessed. Since a preliminary study is seeked and 1D models calibrated on experimental data or CFD results currently represent the cornerstone of design space exploration, a Mean-Line (ML) method is adopted in this thesis. In fact, the use of a resource-demanding method within an optimization loop would not be suitable. In this sense, the ML solution is more attractive. It has more limited accuracy when used alone, but reduces requirements of computational resources and of inlet geometry data as well. Moreover, the distortion impact assessment method employed differs from the past *parallel compressor* technique, as whatever type of distortion can be basically simulated due to the radial and circumferential grid division [23, 24]. Therefore, analysis and design under BLI conditions are achievable. In this work, a distortion pattern which can be encountered by REC layouts is applied. The next chapter describes how it is imposed and how the subsequent design optimization is realized. Essentially, this latter exploits genetic algorithms by which the most important blade geometric parameters are varied to optimize some performance objectives. The clean study is complete with CFD comparison, while the aim for the distorted case is to conduct the analysis and the design process, introducing the CFD setup which will be used in future works.

Anyway, the general goal is to evaluate the agreement between low-order results and CFD calculations in order to assess the preliminary prediction and plant the seed for further developments of the design optimization process.

Chapter 2

Methodology

In this chapter the methods adopted during the work are described. They represent the core of the thesis and are examined both theoretically and applied to the case considered, the NASA/GEAE R4 transonic fan rotor. A multi-fidelity approach is followed, using ML method and CFD, in order to get a comparison of the results obtained with different levels of accuracy and computational effort requirements.

2.1 Mean-Line solver

SATURN (Systematic Analysis of TURbofaN) is a 1D ML code programmed in C++ in Linux environment by COMETES research group at the University of Padua. It works in analysis mode to provide a quick look at key aerodynamics design and off-design performance of axial compressors, during the conceptual design process. In this phase, a cheap computational procedure is preferred over results accuracy. The foundations of this model are based on the hypotheses made and 1D equations used. Before dealing with that, it is important to comprehend the control volume which is considered by the ML code. This is represented in Figure 2.1, where three areas of interest can be immediately noted: inlet, blade and outlet regions. It will be useful later to describe the software implementation as well.

Returning to the previous discussion, the following fundamental **assumptions** are considered [24]:

- no radial flow is modelled;
- the flow is resolved only at inlet and outlet planes of each region;
- the working fluid is air in standard conditions, hence $k = 1.4$ and $R = 287 J/kgK$;
- angles on the circumferential blade-to-blade plane are referred to the axial direction;
- all variables are calculated for each span of each bladed row, unless otherwise noted (e.g. average variables).

Another key point in this first part is the examination of the most important and **fundamental equations** in fluid mechanics as well as thermodynamics, upon

which the model is based [24]. Indeed, understanding and analysing the performance of aero engines requires a closed set of governing equations, expressing the conservation of mass and energy, linear and angular momentum, entropy as well as several compressible flow relations that govern the isentropic flow. For understanding the basic physical phenomena, the working fluid is modelled as a *perfect gas* and, apart from the rotating elements (fans or compressors), the flow is assumed one dimensional, and its properties vary only in the flow direction. Complex flow phenomena and 3D effects are left to higher computational methods.
Thermodynamics is a crucial topic in the study of compressible flows, since in a high-speed flow energy transformations and temperature changes play dominant roles. Therefore, determining the thermodynamic state before and after the blade region is the initial objective. First, the blade reference frame must be defined. The analysis is conducted considering:

1. the *absolute reference frame*, which is fixed and coincident with the frame of the machine;

2. the *relative reference frame*, which rotates with the rotor.

In Figure 2.2 the rotor velocity triangle is reported, together with the stationary and relative frame, which are the same for a stationary blade. If the blade row is rotating, relative flow quantities are considered.

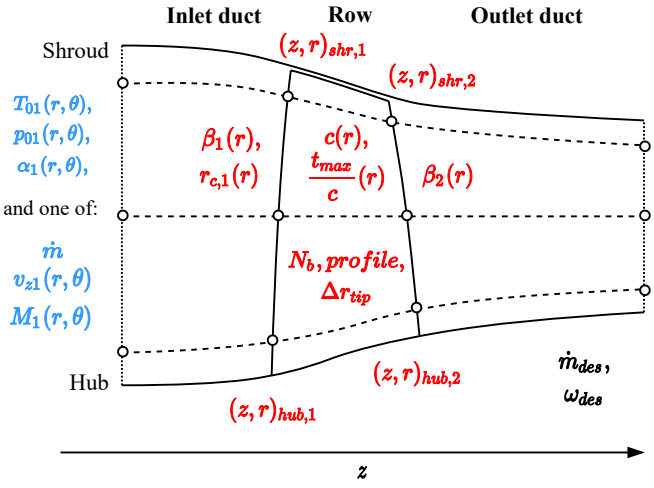

Figure 2.1: *Meridional view of the control volume, with three spanwise positions depicted by dotted lines. In blue, the boundary conditions set at the inlet; in red, the blade geometric features; in black, the design operating conditions. The thermodynamic states are calculated at the circle points and the z direction represents the rotational axis, that points from inlet to outlet.*

The static quantities (i.e., static temperature, static pressure and static density, respectively) are given by Equation 2.2 to Equation 2.4 as a function of Mach coefficient K_M, expressed by Equation 2.1. The ML solver yields these results on a user-defined number of spanwise positions N_r, after n iterations on relative Mach number M_{rel} until convergence.

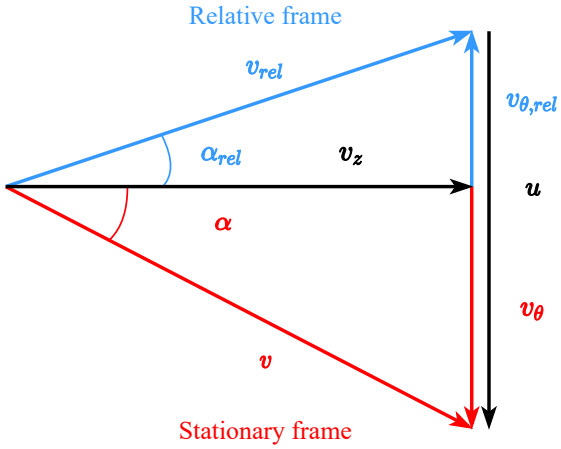

Figure 2.2: *Velocity triangle with the two reference frames.*

$$K_M = 1 + \frac{k-1}{2} M_{rel,n}^2 \tag{2.1}$$

$$T = T_{0,rel} K_M^{-1} \tag{2.2}$$

$$p = p_{0,rel} K_M^{\frac{-k}{k-1}} \tag{2.3}$$

$$\rho = \frac{p_{0,rel}}{R T_{0,rel}} K_M^{\frac{-1}{k-1}} \tag{2.4}$$

The conservation of mass and the known mass flow allow defining the axial velocity as pointed out by Equation 2.5. In addition, a blockage factor ξ is introduced to consider the reduction in flow area along the machine axis. The phenomenon is due to the thickness of the boundary layer on hub and shroud. Then, the flow velocity is defined by Equation 2.6 as a function of axial velocity or flow angle from boundary conditions.

$$v_z = \frac{\dot{m}}{\rho A \xi} \tag{2.5}$$

$$v_{rel} = \begin{cases} \sqrt{v_z^2 + v_{\theta,rel}^2}, & \text{duct outlet} \\ \dfrac{v_z}{\cos(\alpha_{rel})}, & \text{otherwise} \end{cases} \tag{2.6}$$

As regards the iteration loop previously introduced, the next Mach number is weighted considering the relaxation factor φ_M and is calculated following a Newton-Raphson scheme:

$$f(M_{rel,n}) = v_{rel} - M_{rel,n} \sqrt{k R T_{0,rel}} K_M^{-0.5} \tag{2.7}$$

$$f'(M_{rel,n}) = -\sqrt{k R T_{0,rel}} K_M^{-1.5} \tag{2.8}$$

$$M_{rel,n+1} = \varphi_M \left(M_{rel,n} - \frac{f(M_{rel,n})}{f'(M_{rel,n})} \right) + (1 - \varphi_M) M_{rel,n} \tag{2.9}$$

From Equation 2.10 to 2.13 the components of the velocity triangle in the stationary frame are expressed:

$$u = \begin{cases} wr, & \text{rotor} \\ 0, & \text{otherwise} \end{cases} \tag{2.10}$$

$$v_\theta = |u - v_{\theta,rel}| \tag{2.11}$$

$$v = \sqrt{v_z^2 + v_{\theta,rel}^2} \tag{2.12}$$

$$\alpha = \text{atan}\left(\frac{v_\theta}{v_z} \right) \tag{2.13}$$

From the isentropic flow relations, total quantities are computed through the equations below. More in detail, if the blade is rotating, total enthalpy change coincides with the turbomachinery work as indicated in Equation 2.15. Absolute Mach number is found in Equation 2.17.

$$T_0 = \begin{cases} T_{01} + \dfrac{\Delta h}{c_p}, & \text{rotor outlet} \\ T + \dfrac{v^2}{2c_p}, & \text{otherwise} \end{cases} \tag{2.14}$$

$$\Delta h = u_2 v_{\theta 2} - u_1 v_{\theta 1} \tag{2.15}$$

$$p_0 = p \left(\frac{T_0}{T} \right)^{\frac{k}{k-1}} \tag{2.16}$$

$$M = \frac{v}{\sqrt{kRT}} \tag{2.17}$$

One of the most meaningful parameters in fluid dynamics is the Reynolds number (see Equation 2.18), that is physically a measure of the ratio of inertia forces to viscous forces in a flow. The dynamic viscosity is derived from the Sutherland equation, expressed by Equation 2.19.

$$R_e = \frac{\rho v c}{\mu} \tag{2.18}$$

$$\mu = 1.458 \cdot 10^{-6} \frac{T^{1.5}}{T + 110.4} \tag{2.19}$$

ML solver includes also empirical correlations for different **losses** in order to close the equation system. In fact, in addition to the previously mentioned blockage factor, other terms need to be modeled. They are total pressure losses $\Delta p_{0,loss}$, rising

from the interaction between the flow and the blading, and the deviation angle δ, rising from the mixing between pressure and suction side flows.

$$p_{02,rel} = p_{01,rel} - \Delta p_{0,loss} \tag{2.20}$$

$$\alpha_{2,rel} = \beta_2 + \delta \tag{2.21}$$

The loss models implemented are summarized in Table 2.1 and are briefly described below. For further explanations see [24].

- Blockage: reduction of the flow passage area, due to the boundary layer formation at the blade surfaces. In detail, some studies [25] claim that the hub displacement thickness increases from the front to rear area, whereas the shroud displacement thickness remains almost the same;

- Reference incidence angle: the incidence angle at minimum losses conditions. It is defined as the combination between the incidence of a 2D cascade and the effect of 3D geometry;

- Reference deviation angle: the deviation angle at minimum losses conditions. This quantity is the difference between the blade camber angle and the flow angle at the Trailing Edge (TE), due to the flow deflection;

- Profile losses: losses caused both by the stream tube contraction, typical of compressors, and by the effect of the boundary layer on the suction side and pressure side of the blade, which creates drag. These losses are typical of viscid fluids;

- Shock losses: the supersonic flow generates intense shock waves and as consequence shock losses. As known, entropy increases and a total pressure loss happens. Shock loss models account for this phenomenon;

- Endwall losses: the end wall flows cause loss through viscous shear and through mixing with the mainstream flow in the blade passage. In addition, they interact with the boundary layers on the blade surfaces, potentially causing further loss;

- Secondary losses: losses coming from secondary flows;

- Tip clearance losses: this loss is associated with leakage flow over the tip and hub clearances and highly depends on whether the blades are shrouded or unshrouded;

- Off-design losses: this model comes into play for the machine in off-design conditions. The first important change, with respect to the design configuration, is the incidence angle. When the diffusion levels on the blade surfaces become too high, the flow separates leading to excessive loss and possible stall or surge;

- Surge detection: it is assumed through the combination of two models. When the concept of stall share is not satisfied, the surge is modelled to occur when the static density ratio between outlet and inlet reaches its maximum value;

- Choking detection: it happens when the Mach loop diverges. The concept of choke share is also added.

LOSS TYPE	MODEL
Blockage	Smith [26]
Ref. incidence angle	Lieblein [27], Çetin et al. [28]
Ref. deviation angle	Lieblein [27], Carter [27], Çetin et al. [28]
Profile losses	Lieblein [27], Koch and Smith [30]
Shock losses	Miller et al. [31], Koch and Smith [30]
Endwall losses	Koch and Smith [30], Koch [32], Benner et al. [33]
Secondary losses	Howell [34]
Tip clearance losses	Yaras and Sjolander [35]
Off-design losses	Creveling and Carmody [29], Çetin et al. [28]
Surge detection	McKenzie [36], Day et al. [37], Miller and Wasdell [38]
Choking detection	Divergence in M loop

Table 2.1: *Losses sources and their references.*

2.1.1 Software implementation

An insight into the ML software implementation is necessary to understand better the work behind the scenes.

To start off, a general scheme of the code is reported in Figure 2.3. It is composed of three main parts: inputs, solver, outputs. Before starting, it is mandatory to make a premise. In fact, the software has a peculiarity. It has been developed to consider a uniform or non-uniform inlet flow conditions. Therefore, a wide range of flow patterns can be assumed. To do this, the annulus area of the control volume is considered, at inlet or outlet (see Figure 2.4). This surface can be divided circumferentially (θ direction) into different sectors and radially (r direction) into concentric circular annuli. The clean configuration is a particular case of the discretized one. Indeed, it provides only one sector, that corresponds to the entire annulus and through which the flow features are uniform in θ direction. Thus, in this case, a single set of boundary conditions applied to the 1D control volume is enough to yield the fan performance. Different is the distortion case, where the flow behaves non uniformly along the circumference and it is necessary to consider the entire surface. Hence, the BC files used coincide with the number of sectors (a dividend of blades number) which divide the surface. This is the reason why the computational effort is higher. A more detailed discussion is presented in section 2.2.

Inputs
Considering a clean configuration, the code requires the following inputs:

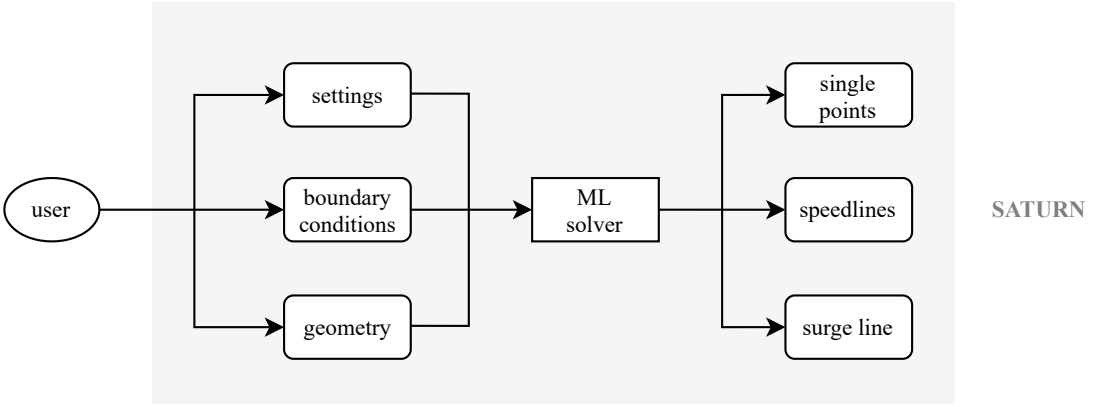

Figure 2.3: *Flow chart of SATURN general structure.*

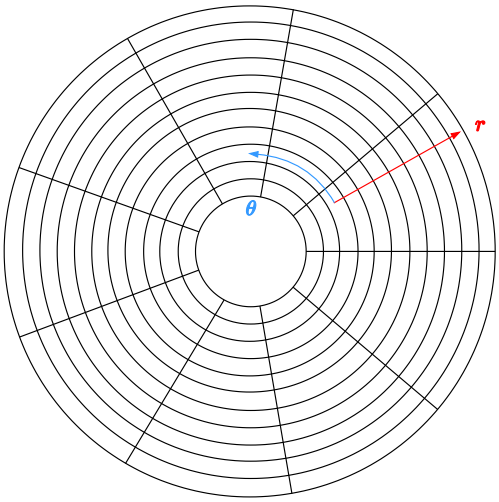

Figure 2.4: *Quasi-2D grid created over the entrance and outlet surface areas by the ML code. The intent is to reproduce the boundary conditions and the effect of a distorted inflow.*

1. Geometry files: files indicating the boundaries of the three bidimensional regions, the blade zone and the two ducts before and after this. For the rotor, other characteristics are reported, as the number of blades, the profile shape and the tip clearance height. Moreover, this file includes the spanwise values of five important variables which define the profile camber line at each span: the blade angle at inlet and outlet, the chord length, the curvature radius of leading edge and the maximum thickness to chord ratio;

2. Boundary conditions files: files describing spanwise variables at inlet. Different BC sets can initialize the code calculation. They all provide the total pressure p_{01}, total temperature T_{01} and absolute flow angle α_1. Then, depending on the set type ($pTam$, $pTav$, $pTaM$, respectively), a fourth variable is added, that is the mass flow, axial velocity or Mach number. The last two cases are implemented for non-uniform inlet conditions, where the mass flow for each cell is not known. Furthermore, in order to obtain a complete compressor

map for the speedline specified, BCs relative to different operating points are needed and two approaches can be followed:

- Multiple single points: given the axial velocity or Mach profile for the design and N off-design points, $N+1$ boundary conditions files are loaded and each point is simulated separately. From each profile a mass flow is extracted;
- Rescaled off-design profiles: given the axial velocity or Mach profile of one operating condition, tipically design or peak efficiency, the corresponding mass flow is calculated. As a first approximation, the profile for an off-design point, with mass flow $\dot{m}$, is obtained rescaling the design profile according to the off-design mass flow, as following:

$$v_z(r) = v_{z,des}(r) \cdot f\left(\frac{\dot{m}}{\dot{m}_{des}}\right) \quad \text{or} \quad M(r) = M_{des}(r) \cdot f\left(\frac{\dot{m}}{\dot{m}_{des}}\right)$$

  Successively, knowing the off-design profiles, the mass flow $\dot{m}$ is recalculated;

3. Settings files:

   - Case specification file: here the features of the studied case are reported, such as design conditions (i.e., mass flow, rotational speed, etc. . .), components included (i.e., fans, IGV, OGV, ducts, stages) and solver tuning parameters;
   - Journal file: this file contains the main instructions and is divided into three sections:
     - Operating conditions: the BC set is chosen, BC files and the approach followed are indicated. Percent speed is defined as well, together with the option for corrected units;
     - Loss sources: the user decides which loss sources to be introduced in the simulation;
     - Solution control: the number of spanwise locations other than the minimum of three is defined. The user can also specify the location of the first streamline and the clustering near hub and tip. If the clustering is zero, a uniform distribution is created. Moreover, there is the possibility of interpolating new geometric data and BC values through the respective instructions. The circumferential discretization is specified through N_θ number of sectors and finally, relaxation factors, numerical tolerance and maximum iterations allowed are chosen. An example is offered in Figure 2.5.

Outputs
The ML solver yields these text files:

1. Performance (i.e., total pressure ratio, total temperature ratio, isentropic efficiency, polytropic efficiency and outlet static pressure) in single points:

- Area-averaged performance at design point;
- Spanwise performance at design point;
- Spanwise performance at user-defined mass flow;

2. Area-averaged performance in multiple points:
   - Speedline files;
   - Surge line file;
3. Log files:
   - Main log file: this file contains all the operations done by the code during the simulation;
   - Thermodynamic states log file;
   - Errors log file.

```
1  ------------------------------------------------------
2  SATURN-1 JOURNAL FILE
3
4  ------------------------------------------------------
5  OPERATING CONDITIONS
6
7  ------------------------------------------------------
8  bcSet                              pressTempAngVel
9  bcFileDesignPoint                  bcProfilePeak
10 bcFileOffDesign                    bcProfilePeak
11 rescaleOffDesignProfiles?          y
12 transonicRegime?                   y
13 runAllMassFlows?                   y
14 massFlowRange              [kg/s]  40.0 49.0
15 massFlowIncrement          [kg/s]  0.1
16 elseWhatMassFlows?         [kg/s]  45.994
17 massFlowSpanwisePlot?      [kg/s]  45.994
18 speedsPercent              [-]     1
19 correctUnits?                      y
20 ------------------------------------------------------
21 LOSS SOURCES
22
23 ------------------------------------------------------
24 blockage                           y
25 deviation                          y
26 profile                            y
27 shock                              y
28 endwall                            y
29 secondary                          y
30 ------------------------------------------------------
31 SOLUTION CONTROL
32
33 ------------------------------------------------------
34 spanCalculation?                   n
35 spanExtra                  [-]     8
36 spanFirst                  [-]     0.025
37 spanClustering             [-]     0
38 interpGeometry?                    n
39 interpBc?                          n
40 sectors                    [-]     1
41 relaxationFactorMachLoop   [-]     0.9
42 relaxationFactorLossLoop   [-]     0.8
43 tolerance                  [-]     1e-6
44 iterMax                    [-]     3000
```

Figure 2.5: *Example of journal file.*

2.1.2 Solver validation

In the first part of the work SATURN is used to analyse the NASA R4 transonic fan. Table 2.2 provides a summary of the design parameters for the modern high-bypass fan, developed by NASA and GEAE and tested in the NASA Source Diagnostic Test aeroacoustic programme [39]. The original module consists also of Outlet Guide Vanes (OGVs), that are not considered in the following dissertation. The code is run setting the *pTav* BC set and the option *rescaled off-design profile*. Therefore, as mentioned previously, the off-design velocity profiles are given by rescaling the axial velocity profile at peak efficiency point. The reference BC file is derived from a CFD analysis of R4 under clean conditions close to peak efficiency [40]. Hence, a single-passage simulation is considered. In the ML solver control, one sector and eleven spanwise positions are imposed.

The outputs are the performance maps * computed for speedlines from 50% to 100% of the design speed and spanwise results at design point (see Figure 2.6). In the first figure, the Total Pressure Ratio (TPR) map is reported and compared to the experimental data obtained for the rotor only. It can be noted a good agreement between them. Indeed, the differences are a couple of percentage points, 1.6-2%. The outcomes of the isentropic efficiency η_{iso} show a similar match. The maximum error is about 1%, even if almost all the speedlines do not follow perfectly the experimental mass flow range.
As regards the spanwise trend, the Total Temperature Ratio (TTR) evolution is represented as well. In all figures the matching is good at midspan, but decreases towards tip and hub. For the TPR profile, variations show the maximum values of 7% around span 0.1 and 5% around span 0.7. A similar trend is found for TTR, with maximum errors of 0.9-2%. Excluding the extreme points, the efficiency profile displays differences below 5%.

Parameters	**R4**
$\dot{m}_{des}$ [kg/s]	45.994
ω_{des} [rad/s]	1325
TPR_{des} [-]	1.488
TTR_{des} [-]	1.13
$\eta_{iso,des}$ [-]	0.924
N_b	22
Profile	MCA
Aspect ratio	2.0
$r_{shr,1}$ [mm]	279.08
$r_{hub,1}/r_{shr,1}$	0.3
Δr_{tip} [mm]	0.508

Table 2.2: *R4 fan design parameters.*

*performance map = plot of the measured fan/stage performance as a function of the corrected fan weight flow for a series of constant fan speed lines along which the mass flow is varied from minimum (stall) to maximum (choking). The extremes have to be avoided during flight.

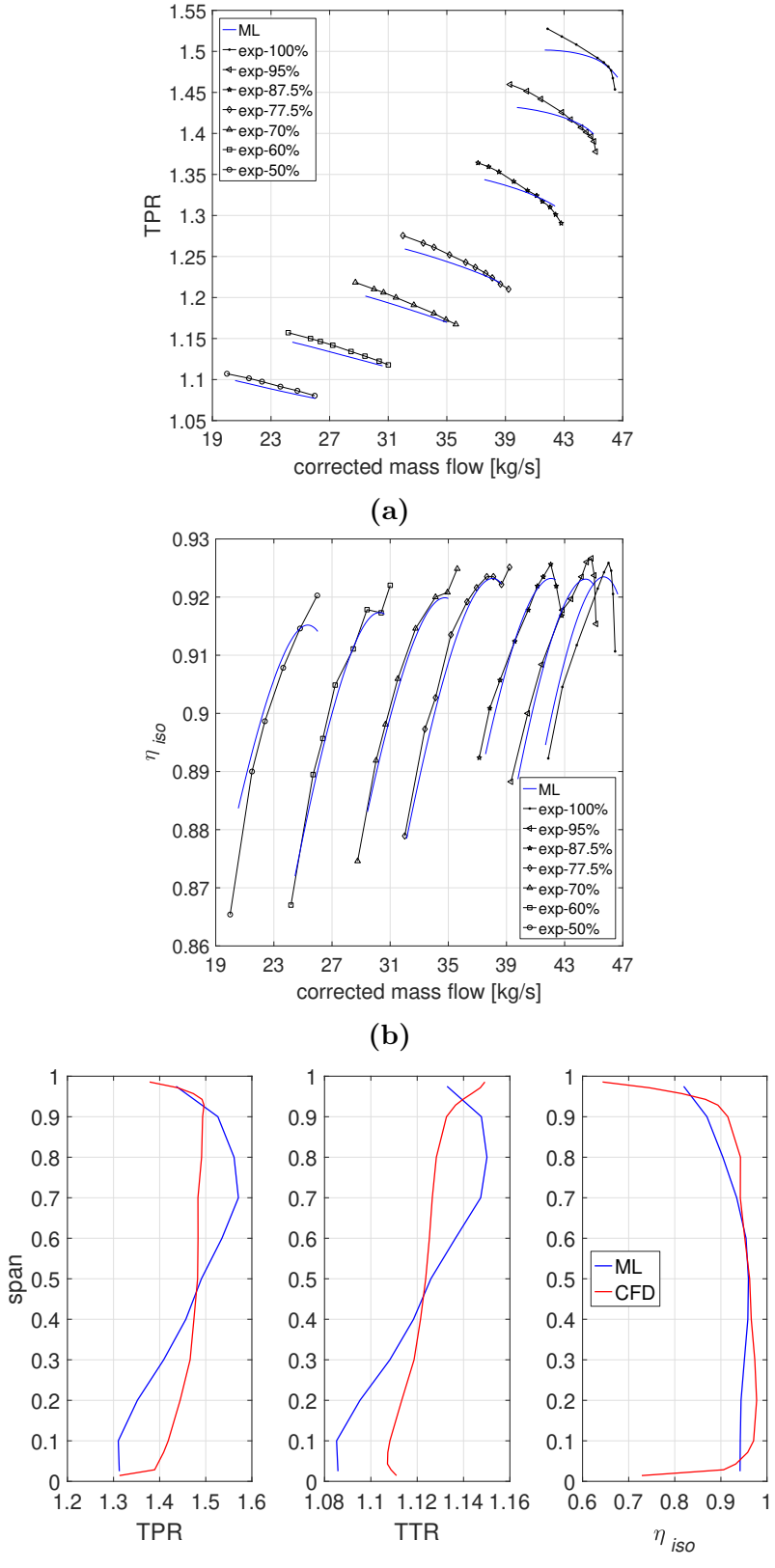

Figure 2.6: *Characteristic maps of total pressure ratio (a) and isentropic efficiency (b) for the baseline geometry of R4. ML and experimental results are compared. At the end, spanwise trends are shown with ML and CFD [40] outputs (c).*

2.2 Inlet flow distortion analysis

The ingestion of non-uniform airflow by an aircraft engine is an ongoing topic, as reported in the introduction. Most of all, this scenario finds application in the modern concepts designed for future aviation, where the engines are embedded in the fuselage. BLI installations will start actively to take hold due to the several benefits offered, but they also create a highly mixed circumferential and radial distortion. Therefore, computational models of low and high order are necessary to evaluate the effect of the present application and to design the various components, as fans in turbofan engines, which are the first components to be affected by this condition.

In this sense, the developed ML code includes the analysis of axial compressors under inlet flow distortion as well. Considering the full-annulus area at the inlet, this distortion could be present both in pitchwise and radial directions, with an axysymmetric configuration or not. The aforementioned airflow condition is introduced and studied through the Discretized Compressor (DC) approach, which is described deeply in the next subsection.

2.2.1 Discretized compressor

DC is an extension of the ML methodology, a strategy adopted to deal with a distortion impact assessment. Here, more than one single sector is considered. In particular, at the inlet, the Aerodynamic Interface Plane (AIP) is divided circumferentially into N_θ sectors and radially into N_r spanwise positions. Referring to Figure 2.4, it is possible to observe the grid considered. Precisely, the number of sectors is defined in order to obtain an integer from N_b/N_θ, where N_b is the number of blades. The discretization is quasi-2D, since every cell is independent from the others. No interfaces exist between spanwise areas and between circumferential sectors, thus discontinuities may occur.

In this thesis, the BCs required by the code derive from the post-processing of full-annulus RANS simulations (see subsection 2.5.3). A file is saved for each sector, that includes the spanwise distribution of different variables, depending on the BC set imposed. As previously described, the sets used in distortion cases can be *pTav* or *pTaM*. Generally, the first is considered, thus the aforesaid variables are total pressure, total temperature, absolute flow angle and axial velocity.

Afterwards, the spanwise performance for each sector and the overall performance (characteristic maps) can be assessed. The latter, such as total pressure ratio, total temperature ratio and isentropic efficiency, are calculated through the averaging yielded by Equation 2.23. In fact, given a variable $\phi(r, \theta)$, at first a circumferential mass flow-weighting at each spanwise position (Equation 2.22) is carried out and, following that, an area-averaging is performed (Equation 2.23).

$$\bar{\phi}(r) = \frac{\sum_{j=1}^{N_\theta} \phi(r, \theta_j)\dot{m}(r, \theta_j)}{\sum_{j=1}^{N_\theta} \dot{m}(r, \theta_j)} \tag{2.22}$$

$$\phi = \frac{\sum_{j=1}^{N_r} \bar{\phi}(r_j) A(r_j)}{\sum_{j=1}^{N_r} A(r_j)} \tag{2.23}$$

2.2.2 Sensitivity analysis

The fan rotor investigated in the current thesis is composed of 22 blades. For this reason, only three levels of discretizations can be employed: 2 sectors, 11 sectors or 22 sectors. A sensitivity analysis is conducted in order to appreciate the differences in time and performance, and to decide which grid configuration adopt for the successive design optimization and relative comparison with CFD.

Referring to the total pressure distortion pattern imposed at the inlet during this work (see 2.5.2), a first selection can be made. The spoiled area is included in a wedge of 60° and centred at 180°. Thus, the first option is completely inadequate to even outline the distortion location as well as its shape. The choice falls on the other two available options. In this sense the ML code is run in both cases in order to assess the time required to yield the design speedline and in order to evaluate the performance relative errors with respect to CFD results under distortion inflow at near-peak efficiency. These latter are available in [42] and are also reported in the results chapter. Table 2.3 shows the analysis outputs. Moreover, BC discretization is compared between the two candidates and Figure 2.7 helps to visualize it.

All this information leads to a conclusion. It is clear how 22 sectors allow obtaining the best results, but require a significant computational time considering the application on design optimization. On the other hand, the 11 sectors option does not show excessive discrepancies both in performance and distortion representation, but it is less time consuming. For this reason, it is chosen for the successive design process.

N_r	N_θ	**Time*** [s]	$\mathbf{e_{TPR}}$ [%]	$\mathbf{e_{TTR}}$ [%]	$\mathbf{e}_\eta$ [%]
11	11	131.8	0.2512	0.1706	0.5977
11	22	388.08	0.1077	0.1257	0.5737

* Laptop, Intel® Core™ i7-4510U CPU @ 2.0 GHz, 8 GB RAM

Table 2.3: *Sensitivity analysis about AIP discretization.*

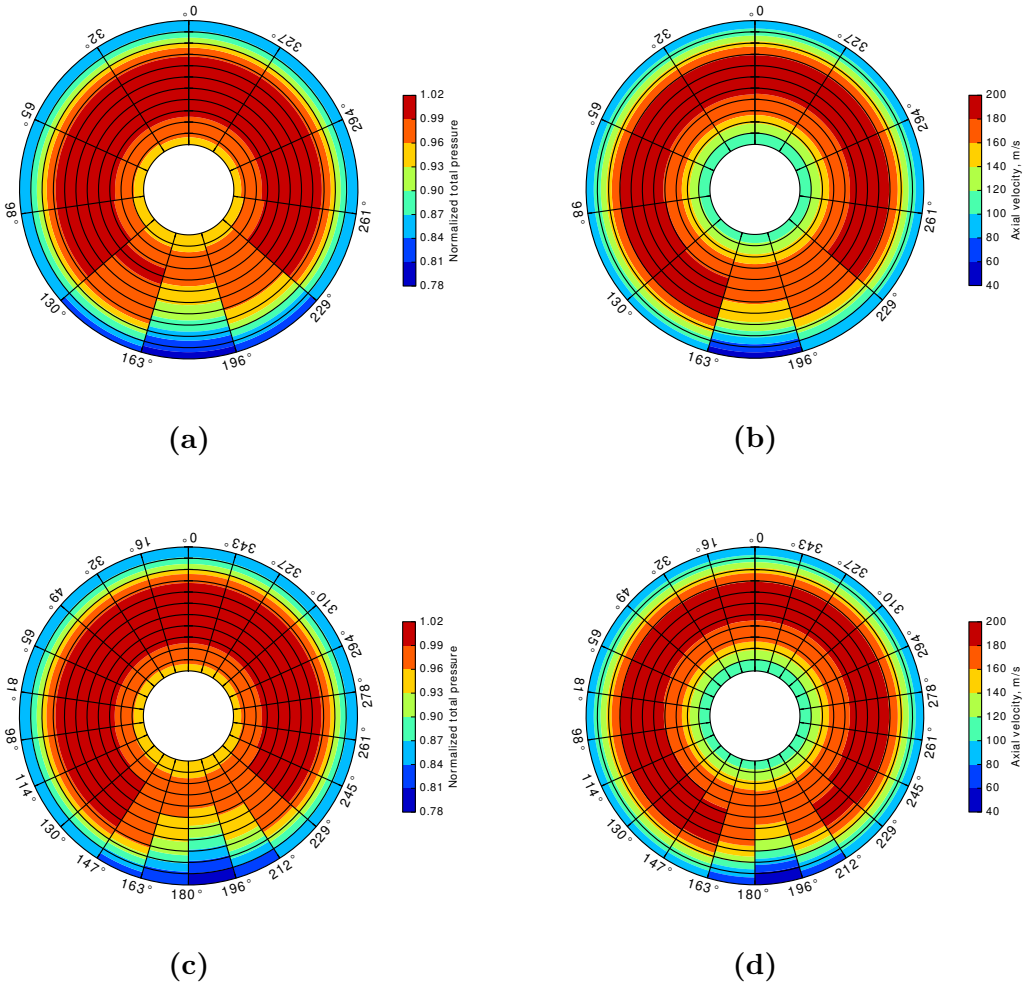

Figure 2.7: *Mean-line BC discretization. Comparison between 11 sectors (top) and 22 sectors (bottom). At the left (a,c) contours of normalized pressure, at the right (b,d) contours of axial velocity.*

2.3 Multi-objective optimizer

Optimization is a procedure of finding and comparing feasible solutions until no better answer can be found. A solution is weighted in relation to an objective to be satisfied. In the industry, this frequently consists for example of minimizing cost of fabrication, maximizing efficiency of a process, maximizing product reliability. Anyway, optimization processes are diffused everywhere, from experiments to engineering design, business decision-making and in our daily life as well.

A first important aspect is to distinguish between a single-objective and a Multi-Objective Optimization Problem (MOOP). The first exists when a problem involves only one objective function, otherwise the job of searching for optimal results is termed as multi-objective optimization. Since the Second World War huge efforts have been made to understand this kind of problems and, at the beginning, MOOP was thought to be simply an extension of single-objective optimization. However, even if similar theories and algorithms can be applied to both, a fundamental difference exists. Considering a two-objective optimization problem, in most cases is not possible to find a unique solution. Indeed, optimizing one goal leads to sacrifice the second best result. A practical example, reported in [43], regards the investigation of the optimal thermodynamic behaviour of subsonic turbojet engines, where 5 different sets, each including two objectives of the output parameters, are considered individually. One of such pairs involves the propulsion and thermal efficiencies, which should be maximized. However, as said before, there is no single optimum solution, because the objectives conflict each other (see Figure 2.8). A gain in the first creates a loss in the second. Trade-off is the key word. Thus, there will be a set of solutions, named *Pareto-optimal solutions*, that find a balance between the existing objectives. This is the fundamental difference between a single-objective and multi-objective optimization task.

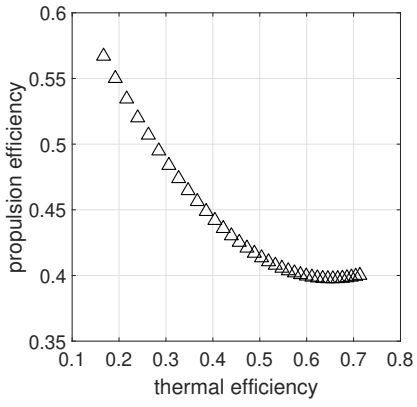

Figure 2.8: *Pareto front of propulsion and thermal efficiencies in two-objective optimization.*

An obvious question can arise *"Among these optimal answers, which solution will I follow?"*. Other considerations must be taken into account. In the first years two main approaches were adopted in classical methods, the ideal approach and the preference-based approach [44]. A scheme that helps to better understand these original techniques is reported in Figure 2.9.

The first path, common to all methods, past and subsequent, consists of building a general mathematical model to represent the MOOP. It is shown in Equation 2.24, with $Q > 1$. It is examined more than one objective function, expressed in terms of a set of decision variables subject to a series of constraints, such as equality, inequality or bounds restrictions. All these limitations are useful to define the decision space S, where feasible solutions can be found. In case of one-dimensional optimization, a single variable is considered, thus $I = 1$.

$$\begin{aligned} Maximize/Minimize \quad & f_q(x) && q = 1, \dots, Q \\ subject\ to \quad & g_j(x) \leq 0, && j = 1, \dots, J \\ & h_d(x) = 0, && d = 1, \dots, D \\ & x_i^{(L)} \leq x_i \leq x_i^{(U)}, && i = 1, \dots, I \end{aligned} \tag{2.24}$$

Looking at the flow chart, the two approaches are sketched. The ideal approach suggests finding a set of trade-off solutions from the initial mathematical problem, giving the same importance to all objectives. After that, by adding further higher-level qualitative information, the user can make a choice. Here, it is clear how the single-objective problem is a particular case of the multi-objective one. In this case, the flow chart is even simplified. The optimizer finds immediately the optimal solution, without the need of other information. Instead, the second approach changes for what concerns the objective functions. In fact, we usually give a different level of importance to each objective. Hence, this technique uses the higher-level considerations to assign a different weight to every single goal and substitutes the initial formulation with a composite objective function. Finally, in most cases it is possible to obtain one optimum solution. A lot of classical methods are based on this last approach, such as the weighted sum approach, the ε-constraint method, the weighted metric methods, the value function model or goal programming methods. Summarizing, the main features of these classical methods are:

- conversion of a MOOP into a single-objective optimization problem;
- no possibility to provide more than one Pareto-optimal solution for each simulation run, thus they need multiple runs to find different Pareto-optimal solutions;
- involvement of user-defined parameters to solve the problem and this is hardly applicable to arbitrary issues.

However, in the last half century, another type of methods has started to spread in solving MOOPs, Evolutionary Algorithms (EA). They are bio-inspired codes, governed by the principles of genetics and natural selection. Bearing in mind that the first goal of a multi-objective optimizer is to find a set of solutions as close as possible to Pareto front (see next subsection), EAs allow satisfying a second goal, that is to find a set of solutions as diverse as possible. This is the great difference with respect to classical methods. A large number of EAs exist. Genetic Algorithms (GAs) are one of them and are deeper described in 2.3.2, since used in the thesis work. In fact, they perform better, with respect to others, in aerodynamic analyses, where an high level of non-linearity is usually present.

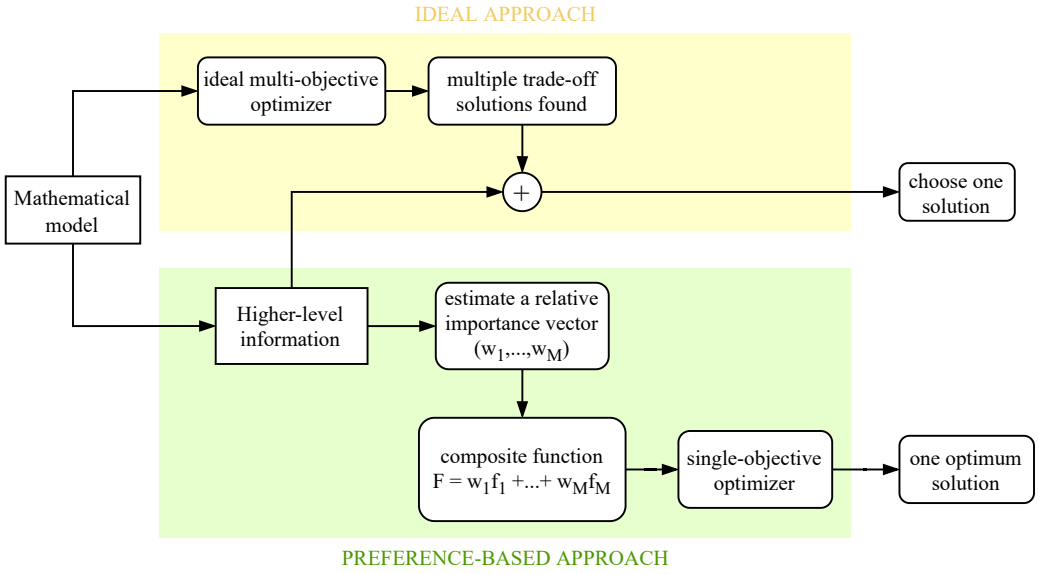

Figure 2.9: *Flow chart of the two main classical methods used to solve MOOPs.*

2.3.1 Pareto-optimality

Most of multi-objective optimization algorithms are developed to find a set of solutions, Pareto-optimal solutions, according to *dominance relationship*. This means that one hypothetical answer x dominates y if it improves at least one objective without worsening the others. For a given set of solutions, the algorithm performs all possible pair-wise comparisons, finds which points are dominated by another, eliminates them and generates a set of optimal solutions. These latter become part of the so-called non-dominated front or Pareto front, that is the space where optimal solutions can be found. It is well reported in Figure 2.10. The red points represent the optimal solutions, whereas the black dotted line corresponds to the Pareto front.

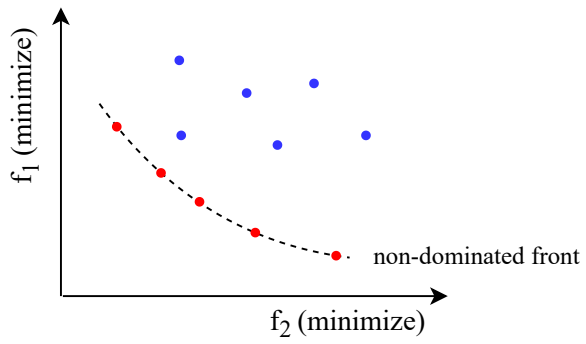

Figure 2.10: *Example of a bi-objective optimization problem. View of a set of solutions and the non-dominated Pareto front formation.*

2.3.2 Genetic Algorithms

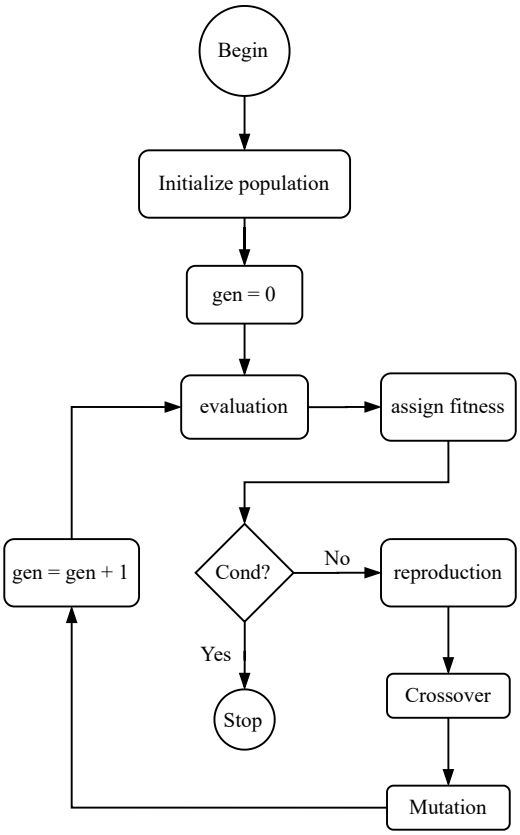

Figure 2.11: *Steps followed by GA to find the optimal solutions [44].*

GAs are one of the most common evolutionary algorithms used for optimization problems and MOOPs [45]. They mimic the concept of genetic inheritance and Darwinian natural selection in living organisms. The strong species have greater opportunity to reproduct and pass their genes to future generations. As mentioned before, these algorithms attempt to achieve two conflicting goals:

- Convergence: find a set of solutions which lie on the Pareto-optimal front;
- Diversity: find a set of solutions as diverse as possible in order to represent the entire range of the Pareto-optimal front.

Many different GAs have been developed to improve these two aspects. The code created by COMETES research group to design axial compressors or fans (2.3.3) presents a GA. In the present application, it is used to optimize the R4 fan under clean and distorted conditions. The optimization considers two objectives, namely maximum total pressure ratio and isentropic efficiency. The decision variables involve only the spanwise geometry of the blade, except for the curvature radius at the leading edge, since its influence is of secondary importance [46]. Moreover, as regards the bound restrictions, the variables are allowed to vary of a fixed percentage of their respective baseline values.

Anyway, the steps followed during the searching of solutions are presented in Figure 2.11 and are described more in detail below [24, 46]. The algorithm starts from an initial population and will generate new individuals iteratively until a desired solution is found.

Initial population
The population, or generation, is initialized by Latin Hypercube Sampling (LHS), a randomly sampling that avoids the gathering of samples around a specific point and guarantees a more homogeneous distribution. The population consists of N_{ind} individuals, candidate solutions, which number is user-defined. A suggested value is $N_{ind} = (2 \div 4)N_x$, where N_x is the number of geometric variables. Each individual, also called *chromosome*, contains different values of the variables and is made of binary digits, *genes*, each one controlling a feature of the chromosome. The greater is the number of bits, the more accurate is the conversion from natural values to binary string, that represents the individual.

Fitness Function
Given the string of an individual, it is necessary to evaluate the solution. In this sense, a fitness function is introduced, based on optimal objectives and constraints. During the optimization process, this function has to be minimized, and assigns to each individual a fitness value, that represents the possibility to survive for the next generation. Therefore, a solution with a smaller fitness value compared to another solution is better. After that, a termination condition is checked. If not satisfied, a new population is created from the previous, with the three next main operators.

Selection
The reproduction operator aims to identify the best individuals in a population. This is the first step of creating the next generation. Some common methods are *tournament selection*, *proportionate selection* and *ranking selection*. In the first case, a series of pair-comparisons are conducted between solutions, based on fitness values. The bests are named *parents* and are selected for reproduction.

Crossover
The creation of new individuals, called *offspring*, is performed by crossover and mutation operators. As regards the first, a number of them exist in literature. Generally, two random parents at time are combined to form other two chromosomes, the *children*. In practice, the first two strings exchange some parts, creating two new strings. In this way, the parents genes are inherited and fitter solutions are obtained. By proceeding iteratively, the overall genes tend to be similar and the solutions tend to cluster. Therefore, to allow more homogeneity, mutation operator is introduced.

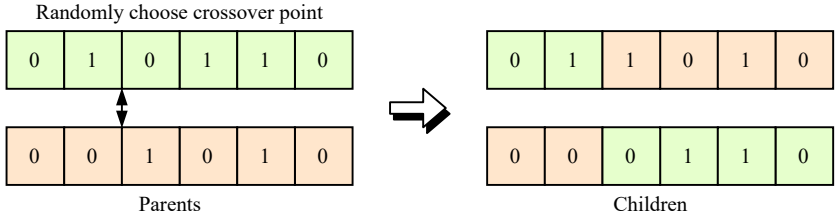

Figure 2.12: *Single point crossover.*

Single point crossover is shown in Figure 2.12.

Mutation
The mutation operator modifies some *children* in order to keep diversity in the next population and avoid excessive clustering of solutions. It is generally applied at the gene level and changes bits, with a user-defined probability. An example is shown in Figure 2.13. However, the operator is introduced not to alter excessively the original string, but with the only purpose of assisting the search escape from local optima.

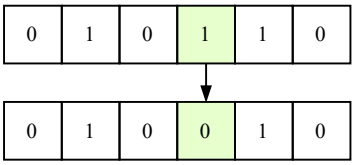

Figure 2.13: *Mutation.*

Elitism
A fraction of the non-dominated solutions discovered during the optimization are defined as elit solutions. In multi-objective GAs, elitism is implemented for two possible reasons, maintaining elite solutions in the next generation or storing them in an auxiliary list and reinserting them successively.

2.3.3 Software implementation

NOPTURN (Numerical OPtimization of TURbofaN) is an optimization code developed in Matlab by COMETES research group for the preliminary design of axial compressors and fans. The general intent is to introduce changes in the blades spanwise geometry in order to obtain better performance. In this case, the objectives to be maximized are the total pressure ratio and the isentropic efficiency. The need for analysing the geometries found during the process leads to the coupling between NOPTURN and SATURN, as shown in the flow chart 2.14. At the end of the optimization, the software will provide the Pareto-optimal individuals to the user. Among these, one yields the best TPR, whereas the other reports the best isentropic efficiency, both respecting the different constraints.

The chosen optimization solver is *gamultijob*. It is provided by Matlab Global Optimization Toolbox and finds Pareto front of multiple fitness functions using GA. This optimizer takes action for two purposes. The first consists of finding the best parameterization of the spanwise curves related to the four geometric variables (blade angles at inlet and outlet, chord length and maximum thickness to chord ratio). In this way, the number of decision variables is reduced, and the problem size is consequently lowered. The iteration process would have to deal with N_r values for each of the four geometric features. The objective is to replace this amount of variables with the control points coordinates of Bézier curves, which have to reproduce the original trends as closely as possible. Therefore, once the four baseline geometric distributions are parameterized in the best way by means of the optimizer, the successive iterations, needed to achieve the performance objectives,

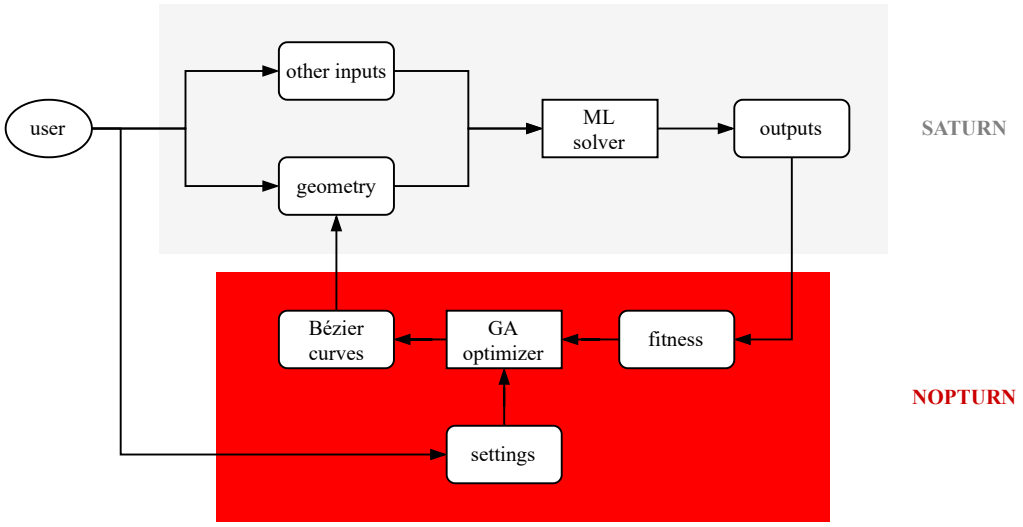

Figure 2.14: *Flow chart of NOPTURN general structure and its link with SATURN.*

will involve these Bézier coordinates, reducing the number of variables. To clarify, a Bézier curve is a parametric curve that uses the Bernstein polynomial as a basis and is modelled through its control points or Bézier points, as shown in Figure 2.15. In this application, 4 or 5 points are considered, depending on the case and accuracy desired. As regards the number of new variables, given that each point has two coordinates, that the extreme points can vary only along the x-axis and considering that is possible to lock x or y variations, the geometric variables can be 4-6 or 5-8 for each geometric distribution, working with 4 or 5 points respectively. Moreover, this change of variables allows also obtaining continuous geometric profiles in output. Indeed, since the ML solver does not model any radial interference, the optimizer could produce jigsaw profiles without a proper parameterization approach.

Once the parameterization is available, the GA is applied for the second and most important task, namely to minimize the fitness function, dependent on the inverse of performance objectives and on the different constraints. The initial population includes the baseline geometry and each individual is identified by a vector of decision variables, *decvar*, used subsequently to build the relative Bézier curves. During the iteration process, some individuals can be excluded for different reasons: geometry out of set boundaries, invalid performance at design point, operating range not including the design mass flow, surge not detected, stall share at surge above 0.3. Moreover, an individual is marked as clone if the difference between its *decvar* and one already analysed is greater than a set tolerance. As regards the fitness function, this is expressed by the following equation:

$$F(x) = f_{obj}(x) + K_p \sum_{j=1}^{N_{con}} P_j(x) \qquad 2.25$$

where the objective function $f_{obj}(x)$ includes the objective variables $\phi_{obj}(x)$ as components. In particular the inverse of these, since the aim is to minimize the fitness

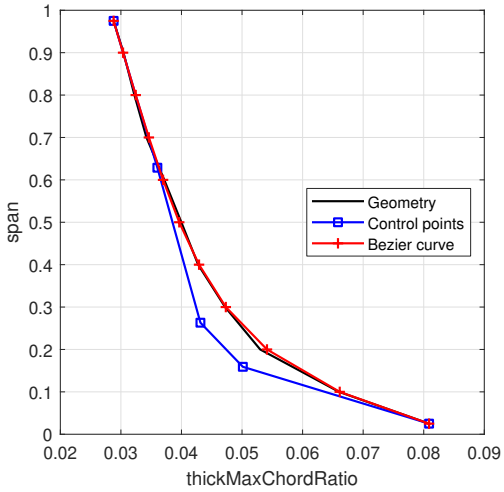

Figure 2.15: *An example of cubic Bézier curve together with its control polygon, 5 control points.*

expression.

$$f_{obj}(x) = \left[\frac{1}{\phi_{obj,1}(x)}, \ldots, \frac{1}{\phi_{obj,N_{obj}}(x)}\right] \tag{2.26}$$

K_p is the penalty coefficient, that weights the constraints and changes during the iteration process. It gives more flexibility for the first generations and then become increasingly restrictive. The external penalty functions are represented by $P_j(x)$. These are applied for each constraint and affect the fitness of individuals according to the level they do not respect the required limitations.

Back to the software structure, NOPTURN has certain inputs and outputs. These are listed below to offer a more complete overview.

Inputs

- Settings file: in this file the user defines the performance objectives, the constraints (as the level of surge and choke margin with respect to the baseline case), the number of individuals and generations, the number of Bézier points with their relative variations along the axis, the geometry variation bounds and a flag for the calculation of new Bézier curves is present;

- ML results: the ML outputs are essential to assign a fitness value to each individual and let the process go on.

Outputs

- Geometries of the best individuals for each of the specified objectives;

- Pareto front of the optimization, the set of solutions that are non-dominated with respect to each other;

- Bézier parameterization files for the baseline geometry;

- Main log file.

2.4 Geometry reconstruction

The geometry reconstruction is a fundamental procedure that aims to convert the optimized spanwise geometric variables, obtained through the previous code, into the 3D coordinates of the spanwise airfoils. This leads to the successive calculation by means of CFD approach and a final assessment of the optimizer results is allowed. The reconstruction is not an immediate operation, since the camber lines are not known. The camber lines consist of the midlines of airfoils, equidistant from the pressure and suction sides. This is the main reason why a Matlab script was created. Therefore, the first necessary step is to calculate the baseline camber lines. All steps followed are reported here below and image representations are shown in Figure 2.16.

1. The 4 baseline and optimized spanwise geometric variables and the baseline airfoils are loaded. The profiles are rotated in horizontal position and their coordinates are divided into pressure and suction side vectors. This lets to calculate the various camber lines through the averaging between the sides;

2. The profiles are rescaled according to optimum chord. In particular, the camber lines and side vectors are rescaled. Afterwards the thickness of rescaled profiles is yielded;

3. The code parameterizes the rescaled camber lines with 5 Bézier control points, thanks to a genetic algorithm, in order to have a match as better as possible;

4. The parameterized camber lines are reshaped according to known optimum angles and the thickness distributions, rescaled in proportion to optimum maximum thickness to chord ratio, are positioned above the midlines. Then, rescaled sides are rebuilt, except for the curvatures around LE and TE;

5. The LE and TE curvatures are rebuilt through circular arcs, after the definition of centers of curvature;

6. The final profiles are obtained and the output files are written for CFD usage. These contain the profiles coordinates and hub and shroud curves, kept equal to the baseline case.

Figure 2.17a presents the comparison between baseline and optimized profiles after the optimization process under clean conditions. In this case, due to results obtained by the GA optimizer in NOPTURN, the solution with the highest isentropic efficiency is chosen. After the reconstruction, the profiles are imported in ANSYS TurboGrid 16.1 and the same mesh parameters of the baseline case are used to create the new grid in order to obtain comparable results and avoid grid-dependent disrepancies. The importation result is shown in Figure 2.17b

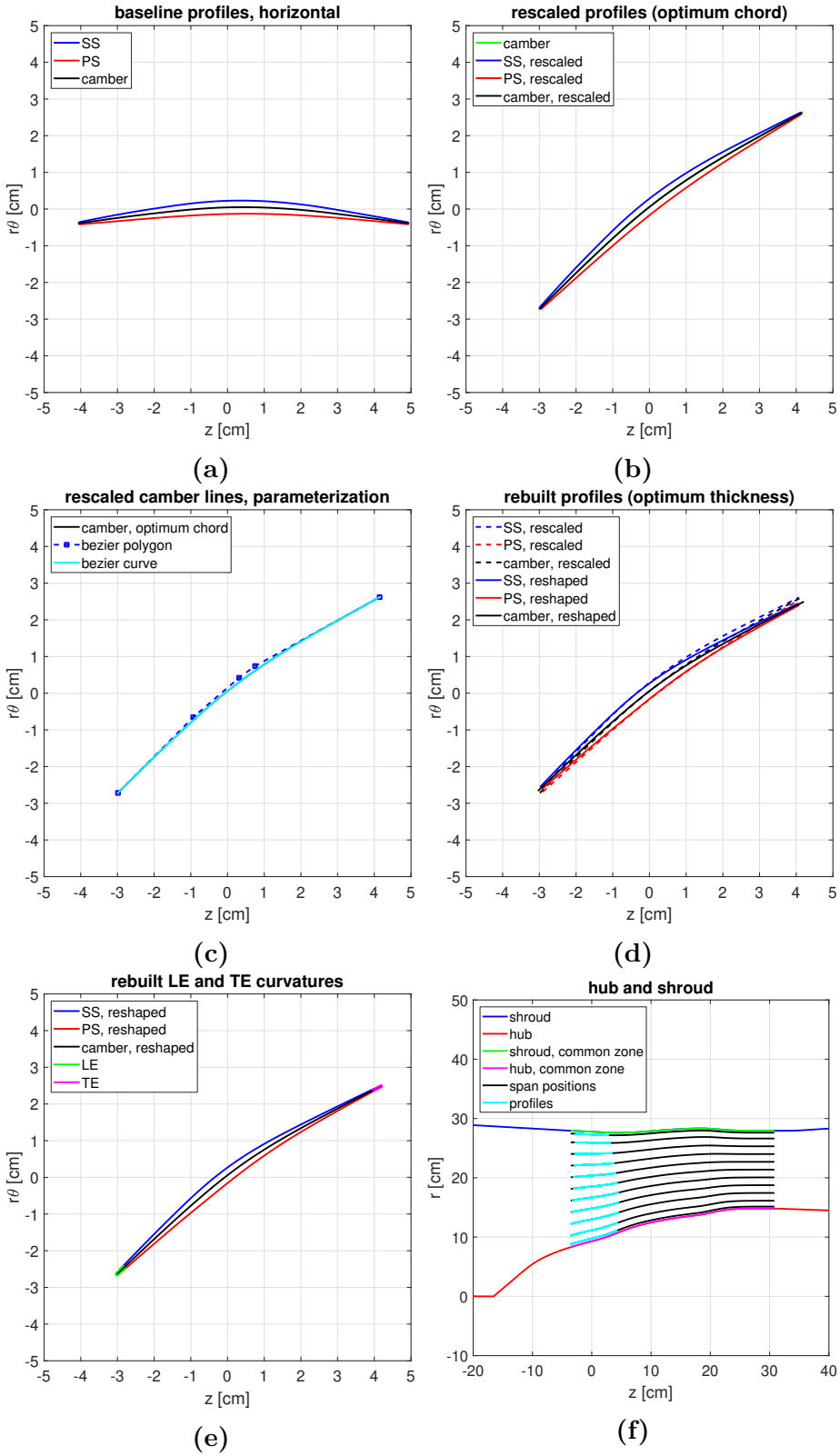

Figure 2.16: *Steps followed by the reconstruction procedure. Profile at span 0.5, optimization under clean conditions. Pressure and suction side definition (a), rescaling according to optimum chord (b), parameterization of rescaled camber line (c), rescaling of sides according to optimum angles and optimum maximum thickness to chord ratio (d), rebuilding of LE and TE (e), profile radial coordinates (f).*

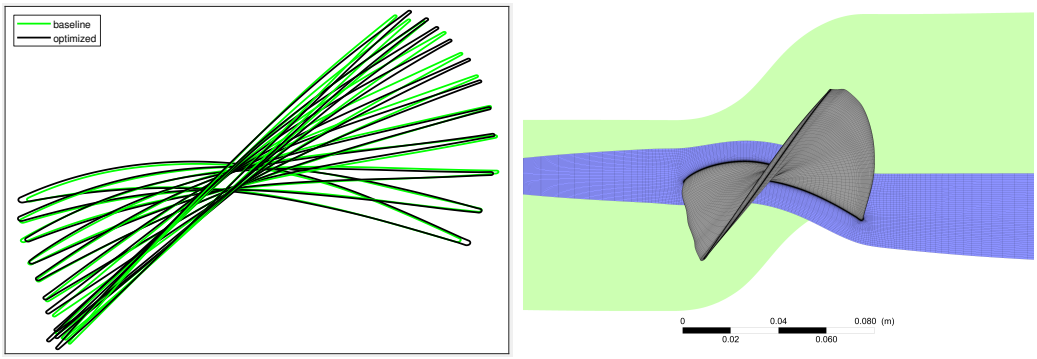

(a) **(b)**

Figure 2.17: *Design under clean conditions. View of the final optimized profiles stacked together (a). Blade geometry obtained in ANSYS TurboGrid after the import and interpolation of the spanwise profiles (b).*

2.5 Computational Fluid Dynamics

Three fundamental principles, namely the conservation of mass and energy and Newton's second law, govern the physical aspects of any kind of fluid flow. These principles can be expressed in terms of full non-linear equations. In their basic form, with the viscosity and thermal conduction terms, they are referred to as the *Navier-Stokes equations*. Computational fluid dynamics is a technique used to replace these complex governing equations with discretized algebraic forms, which are solved to obtain *numbers*. Then, advancing in time and space, a final numerical description of the flow field of interest is guaranteed. Therefore, CFD results are numerical solutions and overcome the lack of analytical solutions. For this reason, many complex aerodynamics problems have been solved through CFD. This approach presents benefits and challenges, that are opposite with respect to that for ML solver.

The main advantage regards the accuracy of results. CFD deals with the full non-linear equations, with the inclusion of detailed physical phenomena. Thus, it can simulate realistic problems with a high degree of reliability. Its role in engineering predictions has become so strong that today it can be viewed as a "third dimension" in fluid dynamics, the other two being the classical cases of pure experiment and pure theory. Obviously, good results are the consequence of a correct setup of the model.

Instead, the computational time is the most relevant drawback. It can be non-negligible for the model preparation, but the dominant component is the computational effort required to obtain the results. This problem is still present, even if increasingly powerful computational resources are available. As regards the model preparation, the flow field is divided into a number of discrete points. The lines connecting these points create a grid and the discrete points are called *grid points*. Successively, the flow properties, such as p, ρ, v, etc. are yielded just at the grid points, after solving the governing equations. The generation of an appropriate grid

for a given problem represents frequently a challenge and it has become a subdiscipline within the CFD method [41].

In the present thesis, this approach is used for two main reasons. The first is to verify the performance of the optimized R4 fan case (targeting maximum efficiency), obtained through NOPTURN and SATURN codes. The design speed is considered and different simulations are run in order to build the compressor map and study the flow behaviour by regulating the static pressure level at the outlet. At first, the clean case is optimized, hence a single passage is analysed, given the axisymmetric and uniform flow field. On the other hand, the full-annulus CFD model is prepared for the assessment of the optimization under distortion. In this way, the results of the low-order optimization procedure are evaluated through a higher-fidelity method. The second reason involves the post-processing of a full-annulus simulation with distortion inflow at design point. In the following work, the aim is to extract the boundary conditions at the inlet, needed to initialize the grid defined by the DC method.

2.5.1 Uniform inflow

The analysis of the fan in clean configuration allows studying only a single-passage domain because of the uniform flow field. Then some results, such as mass flow, will be multiplied by the number of total channels. In the first place, the optimized R4 fan geometry is imported in ANSYS TurboGrid 16.1. Following that, the mesh is generated using the same parameters of a baseline grid validated for previous analyses [40]. This to compare mesh-independent results. The full-annulus geometry and single-passage mesh are shown in Figure 2.18, where the hub curvature near blade denotes the spinner presence.

Different simulations are run, varying the value of the outlet static pressure, in particular increasing progressively the level. This method aims to build the optimized compressor map from choking condition to surge condition. To this end, batteries of three steady RANS simulations, each starting from the previous *.res* file, are launched for each simulated point achieving the convergence of the residuals and performance. The simulations differ for the maximum timescale and maximum iterations, as followed:

1. max. timescale = 1e-6, max. iterations = 1500;
2. max. timescale = 1e-5, max. iterations = 1500;
3. max. timescale = 1e-6, max. iterations = 2000;

The computational time required for the calculation of each point is nearly 4 hours*. The results comparison between CFD and ML are discussed more in detail in 3.2.

CFX-Pre, the physics-definition pre-processor for ANSYS CFX, is used to set the model. The solver settings are described in Table 2.4, while the mesh report is shown in Table 2.5. The information of major interest is outlined.

*Cluster, 80 × Intel® Xeon® E5-2650 0 @ 2.0 GHz, 64 GB RAM

Domain	ALL DOMAINS	Fluid Definition	Air Ideal Gas
		Heat Transfer Model	Total Energy
		Turbulence Model	$k-\omega$ SST
		Reference Pressure	0 [atm]
		Turbulent Wall Functions	Automatic
		High Speed Model	Off
		Domain Motion	Stationary
			(R1 $\rightarrow$ Rotating)
		Angular Velocity	-12657 [rev/min]
	INTERFACES	Interface Models	General Connection
		Frame Change	Frozen Rotor
		Mesh Connection	GGI
Bounds	INLET	Flow Regime	Subsonic
		Flow Direction	Normal to BC
		Total Temperature	288.15 [K]
		Mass And Momentum	Total Pressure
	OUTLET	Flow Regime	Subsonic
		Mass And Momentum	Avg Static Pressure
		Pressure Averaging	Over Whole Outlet
	HUB, SHROUD, R1 BLADE	Heat Transfer	Adiabatic
		Mass And Momentum	No Slip Wall
		Wall Roughness	Smooth Wall
	INTERFACES	Conservative Interface Flux	
Solver Control		Turbulence Numerics	High Resolution
		Advection Scheme	High Resolution
		Compressibility Control	High Speed Numerics
		Residual Target	1e-7
		Residual Type	RMS

Table 2.4: *Solver settings, R4 optimized case.*

Domain	Nodes	Elements
INLET	397010	378432
OUTLET	211990	199584
R1	1684000	1642296
All Domains	2293000	2220312
max y^+	5.915	

Table 2.5: *Mesh report, R4 optimized case.*

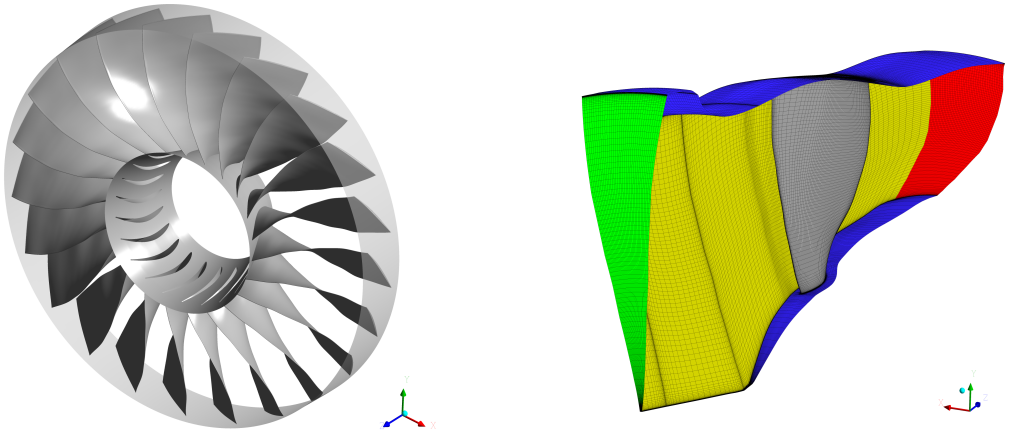

(a) **(b)**

Figure 2.18: *Design under clean conditions. 3D geometry of the optimized R4 fan (a). 3D view of the mesh (b).*

2.5.2 Distortion inflow

Here, the CFD approach is defined for the design under non-uniform conditions. As for the clean case, the geometry defined by the optimization procedure needs to be tested through a high-order method. Here, the procedure followed is described.

First of all, the optimized geometry (see 3.3) is imported using the same *.tst* file used for the baseline full-annulus analysis [42]. This in order to minimize mesh dependence, as said previously. The mesh size corresponds to 1.0×10^6 cells for the rotor passage. Successively, the mesh files of inlet, rotor and outlet domains are imported into CFX-Pre to create the model. The same settings of the clean design are defined. In particular, the *Frozen Rotor* interface model allows reproducing the effect of the inflow distortion, that would be averaged and removed by the mixing plane approach.

Once defined the whole domain, reported in Figure 2.19, the aim is to reproduce a possible inlet condition of a BLI propulsive engine. To this purpose, a total pressure distortion pattern is introduced. It consists of a total pressure drop over a wedged area of 60° and centred at 180°, with a continuous and smooth variation in

order to mimic a realistic situation. In particular, the level and size of the pressure distribution is determined by the following elliptic Gaussian function:

$$f(r,\theta) = \mathrm{A}\exp(-[\gamma(r\cos\theta + x_0) + \lambda(r\sin\theta + y_0)]^2) \qquad 2.27$$

where A is a constant value representative of the minimum total pressure inside the wedge, and is equal to 0.8, whereas γ and λ are equals respectively to $1/2\sigma_x$ and $1/2\sigma_y$ where σ_x and σ_y are the variances, and x_0 and y_0 are constants that control the horizontal and vertical coordinates of the minimum total pressure with respect to the Figure 2.20. This pressure distribution gives a Distortion Coefficient (DC_{60}) value around 0.2 [47].

High-fidelity CFD methods can be used to study the distortion with great accuracy. However, they are very time consuming and, since a preliminary engine design is addressed, only the integral performance are investigated. Therefore, steady RANS simulations with intermediate-fidelity are adequate enough to find the fan rotor characteristic maps. They are used as benchmark to compare the prediction of the leaner low-order tool.

To promote a rapid solution convergence, the first simulation should be initialized from previous results. In this regard, a clean single-passage analysis is conducted in order to obtain a *.res* file at peak efficiency from which starts the distorted full-annulus study.

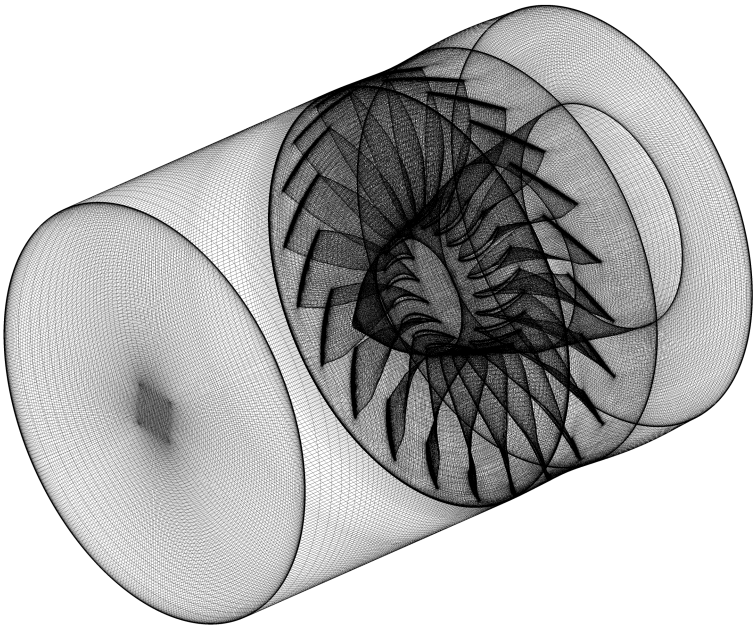

Figure 2.19: *Design under distorted conditions. 3D view of the full-annulus mesh.*

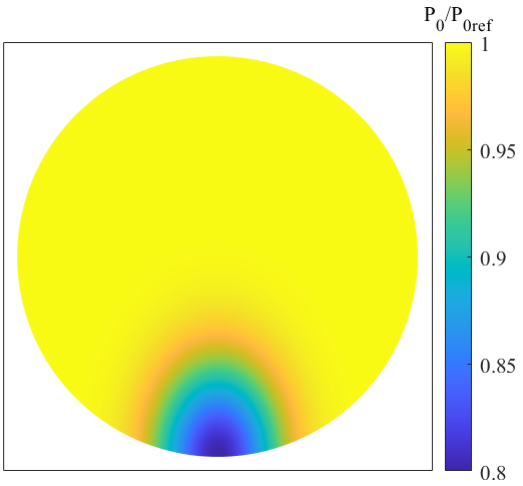

Figure 2.20: *Normalized total pressure distribution at the inlet surface.*

2.5.3 Full-annulus post-processing

The following post-processing involves the full-annulus CFD simulations under distortion inflow. It aims to extract the BCs for the discretization enabled within the ML code and to yield the spanwise performance predicted by the CFD. These are provided for each of the N_θ sectors defined and along the N_r spanwise areas in which the sectors are divided. ANSYS CFD-Post is used to achieve this purpose. However, the hub to shroud turbo charts are not suitable for the present case, since they provide spanwise variables averaged over the full annulus. Therefore, a new automated procedure had to be developed. The planned steps are described here below.

1. The first step is to build two surfaces (*mother surfaces*) placed at the inlet and outlet of an arbitrary channel. Two options exist to create them. In the first case, the user defines two Turbo Surfaces, which positions are determined considering the visualization of the streamlines as support. The inlet area has to centre as many streamlines as possible inside the channel, while the outlet has to capture all the possible incoming streamlines. Otherwise, two polylines, built along the TE and LE of a blade, are imported allowing the creation of the two *mother surfaces*, that correspond to the inlet and outlet of a single channel. An explicative image of the first method, where the inlet surface is positioned over the spinner, is shown in Figure 2.21.

2. Another surface, referred as *moving surface*, is divided into different spanwise areas, equally spaced along radial direction. A value of 50 surfaces is considered.

3. Several variables are defined and averaged on each spanwise area. The BCs required by the ML code are total pressure, total temperature, flow angle and axial velocity. Therefore, these variables are sought.

4. The *moving surface* moves from inlet to outlet sides of each channel, translating and rotating progressively by the same needed angle. During this process the variables of interest are extracted. In particular, for each channel, a file containing the spanwise BCs and a file with the related spanwise performance are saved.

5. Secondly, a Python script is launched. This is created for two main reasons. First of all it provides the pitch-averaged values of the previous variables over the user-defined number of sectors N_θ. Thus, this has to be a dividend of the number of blades. Then the script formats the created files in order to be readable by the ML code.

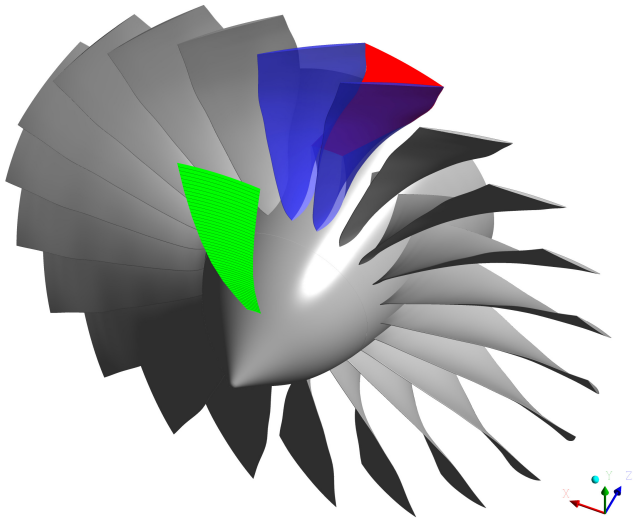

Figure 2.21: *Full-annulus R4. Spanwise subdivision of inlet (green) and outlet (red) surfaces for DC data extraction.*

Chapter 3

Results

The following chapter focuses on the results yielded by the present methodology applied to the NASA/GEAE R4 transonic fan. The chapter is divided into three sections and a comparison between the results of the low-order optimizer and the CFD approach is provided. The first regards the analysis of the rotor under distorted inflow conditions, whereas the last two deal with the design process of the clean and distorted case.

3.1 Analysis under distortion conditions

The following investigation aims to reproduce the distorted incoming flow of a BLI propulsion system, typically present in REC aircraft layout, and to analyse the effects on the performances. The aforementioned total pressure distortion pattern is introduced at the inlet boundary. Before the design optimization process, the baseline NASA R4 transonic fan rotor is studied. The ML and CFD approaches are employed and the distortion influence on performance is examined with respect to the clean case. The baseline CFD results, used as benchmark, are reported in [42], where a deeper overview on the distortion mechanism and on the CFD model preparation is present. The non-uniform flow field was studied by means of full-annulus steady RANS simulations, an accurate approach that anyway is insufficient to correctly measure the interaction of the distortion across the cascades passages. The contribution of the present thesis is the evaluation of the prediction capability of a leaner low-order tool. As said previously, the distorted BCs are imported from the CFD model and the characteristic maps are yielded. During this study, a 11x11 discretization grid is considered.

3.1.1 Performance

In the next pages CFD and ML results are presented. Figures 3.1a and 3.1b show the characteristic maps, where m_{PE} in the x-axis stands for the experimental corrected mass flow at peak efficiency under clean inflow, equal to 46.071 kg/s. The spanwise results at design point, that coincides with peak efficiency point in the code used, are reported in 3.2.

The overall performance maps of the two models are displayed both under clean and distortion inflow conditions. In the first place, the comparison in the distorted case is investigated. Here, CFD results are treated as benchmark, since no experimental data under distortion are available for the assessment. The ML curves are slightly translated towards higher mass flow values with respect to the CFD ones. In this way, the surge and choking mass flows are overestimated. Specifically, the ML code yields an absolute relative error of 0.93% for the surge and 1.67% for the choking mass flows. As regards the performance, a general good match is observed in correspondence of the mass flow at peak efficiency, bearing in mind that this mass flow is different than the baseline one in clean condition and increases mainly in the CFD. In particular, the peak efficiency mass flow predicted by the CFD model is 46.439 kg/s and ML shows a relative error of -1.16%. Anyway, the efficiency values are close, as the ML points out around 0.5% difference. Even the total pressure ratio is similar at that point, with ML showing less than 0.5% difference. Diverse is the situation towards surge and choking conditions. The ML method shows a lower slope than CFD in the TPR trend, thus the average value is higher. In comparison to CFD, the surge point shows a relative error of almost 3%, whereas the choking points almost match perfectly with an approximated value of 1.341. On the other hand, the isentropic efficiency exhibits a more comparable slope between the methods. However, there is an evident discrepancy at choking position. Here, the ML efficiency decreases of 5% from the CFD result. At surge, the ML predicts a greater efficiency than CFD with a relative error of 1.12%.

In the second place, the clean results are highlighted. It is immediately visible the good agreement of the ML and CFD characteristics with respect to the experimental data from near-peak efficiency point to the surge. The TPR and isentropic efficiency predicted through the ML code present mostly lower values than the CFD. At stall, the low-order method commits errors of -1.2% and -2.2%, respectively for TPR and η_{iso}, while at design point the differences are lower than 1%. Different is the situation towards the choking point, where the discrepancies between the methods reach their maximum values. At that point, the CFD model shows a relative error of -12% for TPR and -9.5% for isentropic efficiency. As regards the mass flow values, the difference between the methods tends to increase moving from choke to surge positions.

The comparison between the clean and non-uniform inflow is considered as well. To start off, it is clear how the distortion pattern leads to a large drop in the performance.

First, the CFD is examined. The drop just mentioned equals to 5.5% for what concerns the peak efficiency value and it remains almost constant along the speedline. A similar trend is shown between the two cases. Instead, the TPR map exhibits a worse behaviour. Indeed, the present drop is accentuated by the inversion of the curve slope before the peak efficiency point. The maximum decrease occurs at the surge point and its entity corresponds to 10%. For both performance, the CFD approach yields a similar value of the mass flows at the extremities and a closeness of the results at the choking position.

A similar drop of the performance is observed in the ML results. In this case, the mass flow range moves towards higher mass flows when an irregular inflow is introduced, and the characteristics show an increased curvature. The mass flow

at surge rises of 4.41%, while it increases of 1.87% at the choking position. The greater reduction of the performance occurs in the choking region. However, it does not make much sense to compare the clean choking to the distorted one for ML, since it is evident that this point is not correctly modelled in the clean case. The surge point deserves more attention, as more affected by the distortion phenomenon. Here, the TPR and efficiency losses are 6.6% and 4.5%, respectively. As regards the peak efficiency point, it basically arises at the same mass flow, but the outputs are different. In the distorted condition, the TPR drop is less than 6% and the efficiency decreases of 4.7%.

Figure 3.2 reports the spanwise profiles downstream of the rotor blade, obtained in the distorted configuration at peak efficiency. Some DC sectors are considered. The numbering starts from 0° and follows the θ direction of Figure 2.7a. The discretization with 11 sectors is realized in order to centre the distortion pattern within sector 6. The first sector of Figure 3.2 belongs to a clean region, whereas the other three are positioned around the spoiled area. The three performance are given by the calculation on the sector inlet and outlet sections, and ML and CFD outputs are compared. The TPR shows a good agreement between the two methods at midspan. On the contrary, ML underpredicts the trend at lower span and increases considerably towards the tip, due to a limitation of the shock model. It is particularly clear in sector 6, where the distortion effect shifts the curves to higher pressure ratios above the midspan. The reason is the reduced mass flux, that shifts the local operating point towards the stall and enlarges the compression [47]. This large rise causes a huge TTR and, as a result, an efficiency drop occurs towards tip. The ML isentropic efficiency exhibits a more uniform behaviour in sector 6 and 7, where the discrepancies are reduced with respect to CFD. The underprediction around the tip is present on all sectors. Overall, it can be said that the ML model and the RANS results show an acceptable agreement regarding the overall performance under distortion conditions, hence the analysis tool can be used for design optimization purposes.

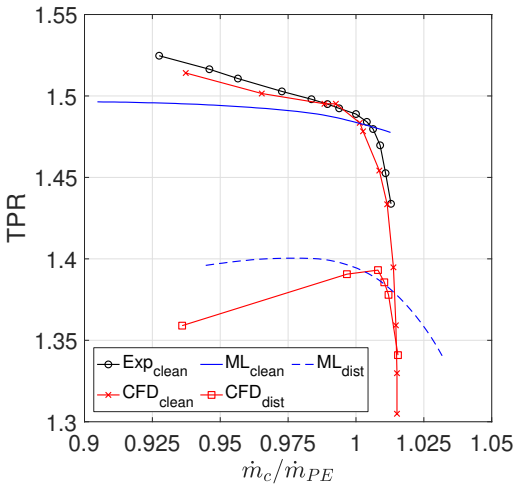

(a)

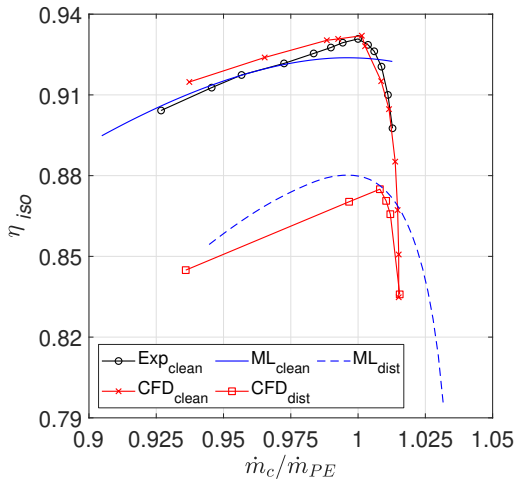

(b)

Figure 3.1: *Characteristic maps of TPR (a) and isentropic efficiency (b) under clean and distorted conditions. ML and CFD results with R4 baseline geometry.*

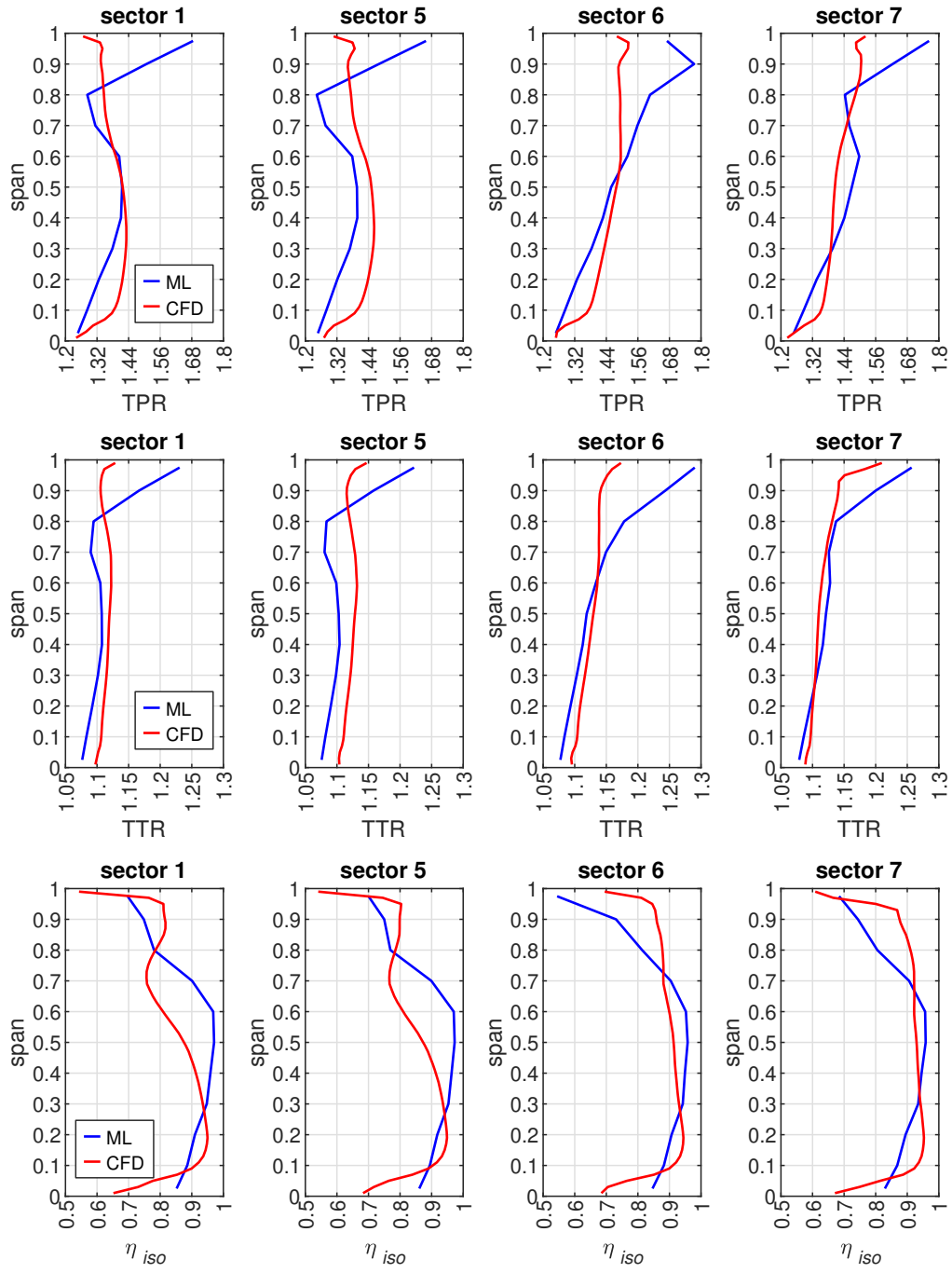

Figure 3.2: *Baseline geometry under distortion configuration. Spanwise profiles downstream of rotor blade for ML and CFD relative to some DC sectors. The numbering starts from 0° and follows the θ direction of Figure 2.7a. Sector 1 belongs to a clean area, the distortion is centred within sector 6.*

3.2 Design under clean conditions

The second part of results regards the design of NASA R4 transonic fan under clean conditions. The spanwise profiles of boundary conditions are uniform in pitchwise direction. Within the ML code, the spanwise trends of BCs are extracted by a RANS simulation at near-peak efficiency, conducted for the baseline geometry. The *pTav* set (see subsection 2.1.1) is considered, as well as atmospheric total pressure and temperature (respectively 101325 Pa and 288.15 K).

The design optimization process is carried out through NOPTURN and SATURN software. As said in the methodology chapter, they create a loop where the first is responsible for the optimization procedure by means of GAs, whereas the second assesses the machine performance obtained for the current geometry. The optimization leads to modify four main geometric variables of the blade along the span, namely inlet blade angle, outlet blade angle, chord length, and maximum thickness to chord ratio. The new geometry determines the final performance. In particular, the GA was built in order to maximize the value of total pressure ratio and isentropic efficiency. Hence, two possible solutions are reported at the end of each optimization process.

In this thesis, a campaign of four optimizations is launched, as indicated in Table 3.1. First of all, constraints on surge and choking margin are imposed. The optimized ones can decrease up to 2% with respect to the baseline case, otherwise the fitness value is penalized accordingly. All the simulations are based on eleven spanwise positions and only one sector, since the flow is axisymmetric. The Bézier curves, that parameterize the spanwise distribution of the four geometry variables, are defined by five control points. Their coordinates substitute the previous geometric variables, calculated for N_r=11 positions along r direction. In this sense, the number of variables decreases. However, the degrees of freedom along x and y axes are not the same in the four optimizations, except for the extreme control points that can move only in x direction.

The first two optimizations do not allow y displacements of the control points, while the translations along x are always accepted. To clarify, the displacement values are reported in Table 3.1 as the percentage ranges admitted with respect to the original coordinate (absolute value). Moreover, the number of individuals increases for the last two runs and, with equal N_{ind}, two incremental numbers of generations are considered. As a good practice, N_{ind} is set between 2 and 4 times the number of variables. Finally, the crossover fraction is equal to 65%.

The second optimization (ID = 2) is chosen for the 3D reconstruction and analysis in ANSYS-CFX. In particular, the selected solution maximizes the isentropic efficiency. One of the reasons for choosing the second ID is the low computational time required, the second-best one, but the main cause concerns the geometric trends, especially the chord distribution. In fact, the four simulations present a clear difference for what regards this geometric variable and ID = 2 shows the most suitable geometry to be studied, since the closest distribution to the baseline case. In Figure 3.3, the comparison between the baseline and optimized geometric variables is reported. The greatest shape difference occurs for the chord. This follows the original curve until span 0.6, where it starts to decrease towards tip. Instead,

the greatest relative differences happen for the inlet and outlet blade angles, mainly above midspan, where the maximum decreases of the optimized ones are respectively of 7% and 10%.

The evolution of the Pareto front is represented in Figure 3.4.

Optimization ID	**1**	**2**	**3**	**4**
Objectives		$\max(\eta_{iso})$ $\max(\text{TPR})$		
Constraints		$\frac{\text{SM}}{\text{SM}_{base}} \geq 0.98$ $\frac{\text{CM}}{\text{CM}_{base}} \geq 0.98$		
$\boldsymbol{N_r}$	11	11	11	11
$\boldsymbol{N_\theta}$	1	1	1	1
Bézier control points	5	5	5	5
Variables	20	20	32	32
Exploration range, x	15%	15%	15%	15%
Exploration range, y	0%	0%	15%	15%
$\boldsymbol{N_{gen}}$	35	50	35	50
$\boldsymbol{N_{ind}}$	60	60	96	96
Crossover fraction	65%	65%	65%	65%
Time [s]	5.74×10^3	8.15×10^3	9.39×10^3	1.29×10^4

Table 3.1: *Optimization settings. Design under clean conditions.*

3.2.1 Performance and blade-to-blade contours

In the next pages CFD and ML results are presented. Figure 3.5 show the characteristic maps and the spanwise results at design point. After that, it is shown a comparison of the contour plots between baseline and optimized cases on the blade-to-blade plane. Below, a description and discussion of the overall outputs is given [48].

Performance. In this case, the comparison with the CFD is not an end in itself step, but the higher-fidelity analysis aims to verify if the optimized geometry yields reasonable results. The outputs of the two methods are reported in Figure 3.5 both under clean inflow conditions, for baseline and optimized geometry. In the first place, the mass flow values are investigated. The optimization shifts the mass flow range towards higher quantities, except for the stall in ML. However, a discrepancy between ML and CFD results exist, especially for the surge point. In both methods the choking mass flow increases. CFD predicts an increment of nearly 2.5% with respect to the original case, reaching 47.93 kg/s, and the ML code overestimates this value with a relative error of 0.95%. The agreement is lower for the surge region.

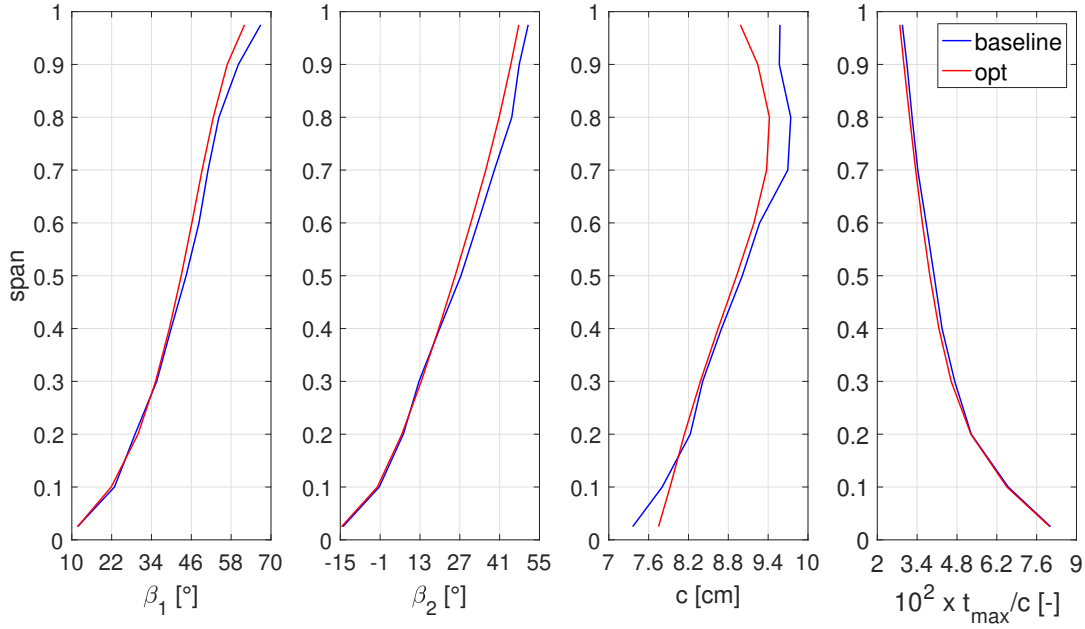

Figure 3.3: *ID=2. Optimized spanwise geometry compared to baseline. From left: inlet blade angle, outlet blade angle, chord length and maximum thickness to chord ratio. Clean case.*

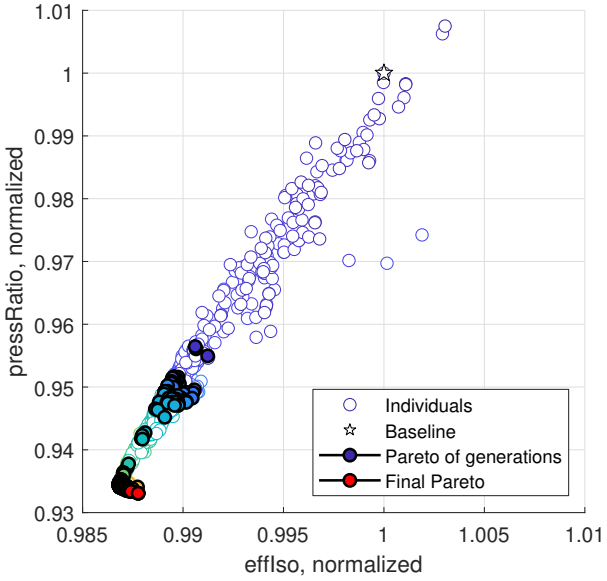

Figure 3.4: *Design under clean conditions, ID=2. Pareto front evolution.*

According to the ML method, this event occurs with a mass flow greater of almost 1% than the baseline. On the other hand, the CFD detects choking for higher mass flow, that is 45.58 kg/s. The ML code points out a relative error of -7.65%. The reason of this difference could be due to the effects not considered by the 1D code, such as 3D phenomena. As regards the optimized near-peak efficiency point, it arises at 47 kg/s in line with CFD forecasting. Meanwhile, the low-order method estimates this maximum at 46.08 kg/s, with a relative error of -1.95%.

The overall performance represented are the total pressure ratio and isentropic efficiency. In CFD-Post, they are calculated considering the outlet variables at one midspan axial chord downstream of the blade. The ML solver yields a TPR improvement of 6.5% and a 1.2% higher isentropic efficiency, with respect to the baseline output at near-peak efficiency point. Considering the entire mass flow range, there is a 6-7% rise of TPR and a 1-1.5% increment of isentropic efficiency. The CFD method shows a rise of 2.9% for TPR and a 0.3% reduction of isentropic efficiency, compared to the baseline curves at near-peak efficiency.

As regards the spanwise performance, the total temperature ratio evolution is represented as well (see Figure 3.5c). Both CFD and ML optimized trends (TPR and TTR) quite follow the baseline curves before span 0.4 and, after that, they start increasing progressively towards tip. The ML solution reaches a 15% and 4.2% maximum rises of TPR and TTR respectively around span 0.9. In the same position, CFD maximum increases are equal to 6% and 2% for TPR and TTR respectively. The matching between the two methods is good at midspan, but decreases towards tip and hub. Before span 0.5, ML maximum relative errors occur at span 0.1, whereas after span 0.5 they take place above span 0.9. Excluding the extreme points, the efficiency profile displays differences below 3% between optimized and baseline case. Towards tip, ML values tend to increase, while CFD curve shows a slight decrease around span 0.2 and span 0.8.

Blade-to-blade contours. The CFD contours on blade-to-blade plane of total pressure and relative Mach number, at near-peak efficiency, are displayed in Figure 3.6 and 3.7 respectively. Three span positions from hub to shroud are examined in order to have a more complete description of the flow behaviour. For the optimized geometry, the total pressure level is enhanced. At the outlet this variable is higher, while a lower value is detected at LE around the suction side due to the incidence effects. Furthermore, a stronger shock wave, orthogonal to the pressure side, is visible at span 0.9, indicating a reduced surge margin towards tip. One of the reasons of this increase at tip is the result of a camber increase due to the reduced blade angles and chord. The relative Mach number results higher as well, in particular at the suction side of LE. On the other hand, the regions of lower speed, such as the outlet wakes, appear to be unaltered.

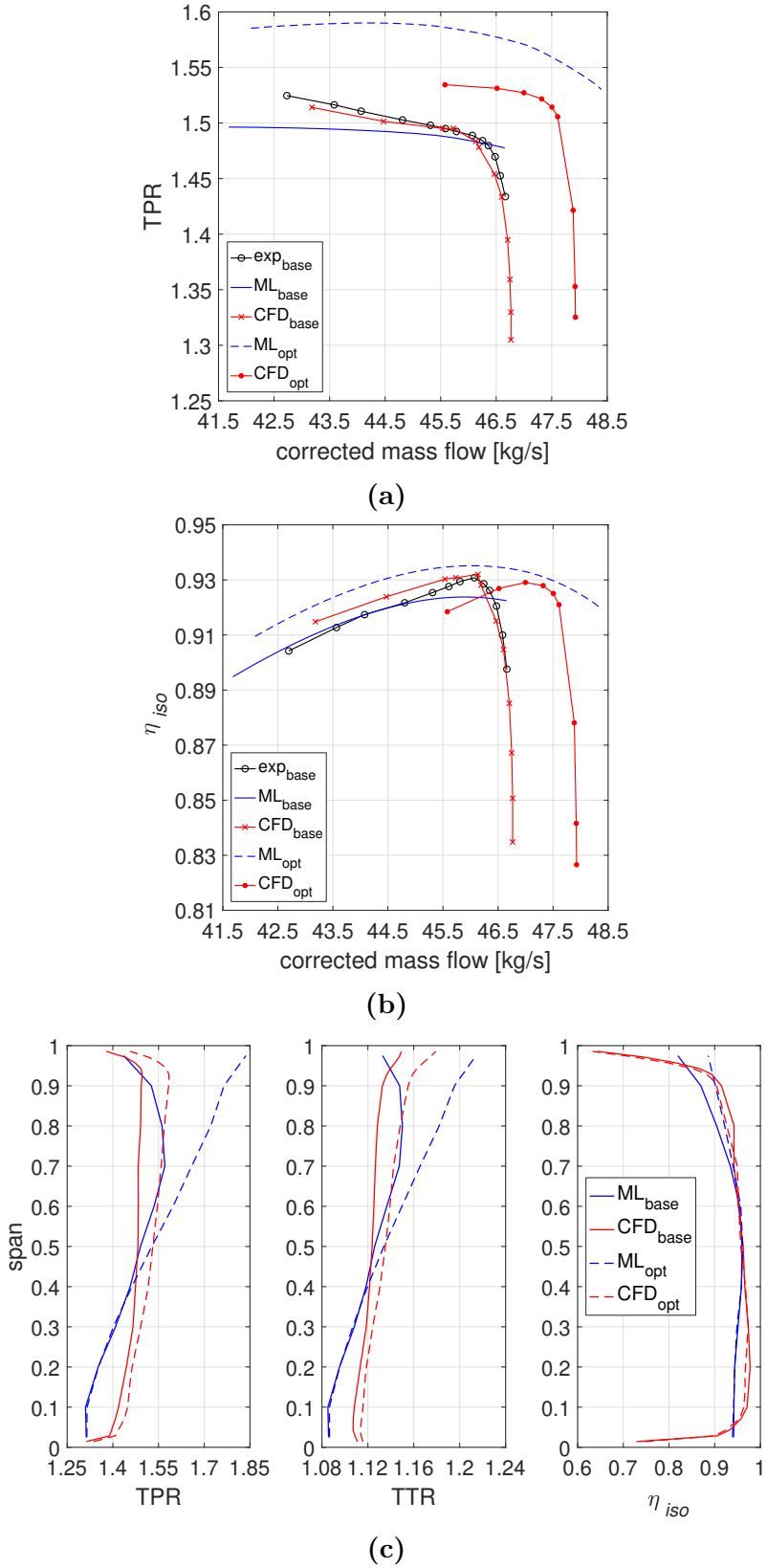

Figure 3.5: *Spanwise outputs (c) and characteristic maps of TPR (a) and isentropic efficiency (b) under clean conditions. ML and CFD results with baseline and optimized geometry.*

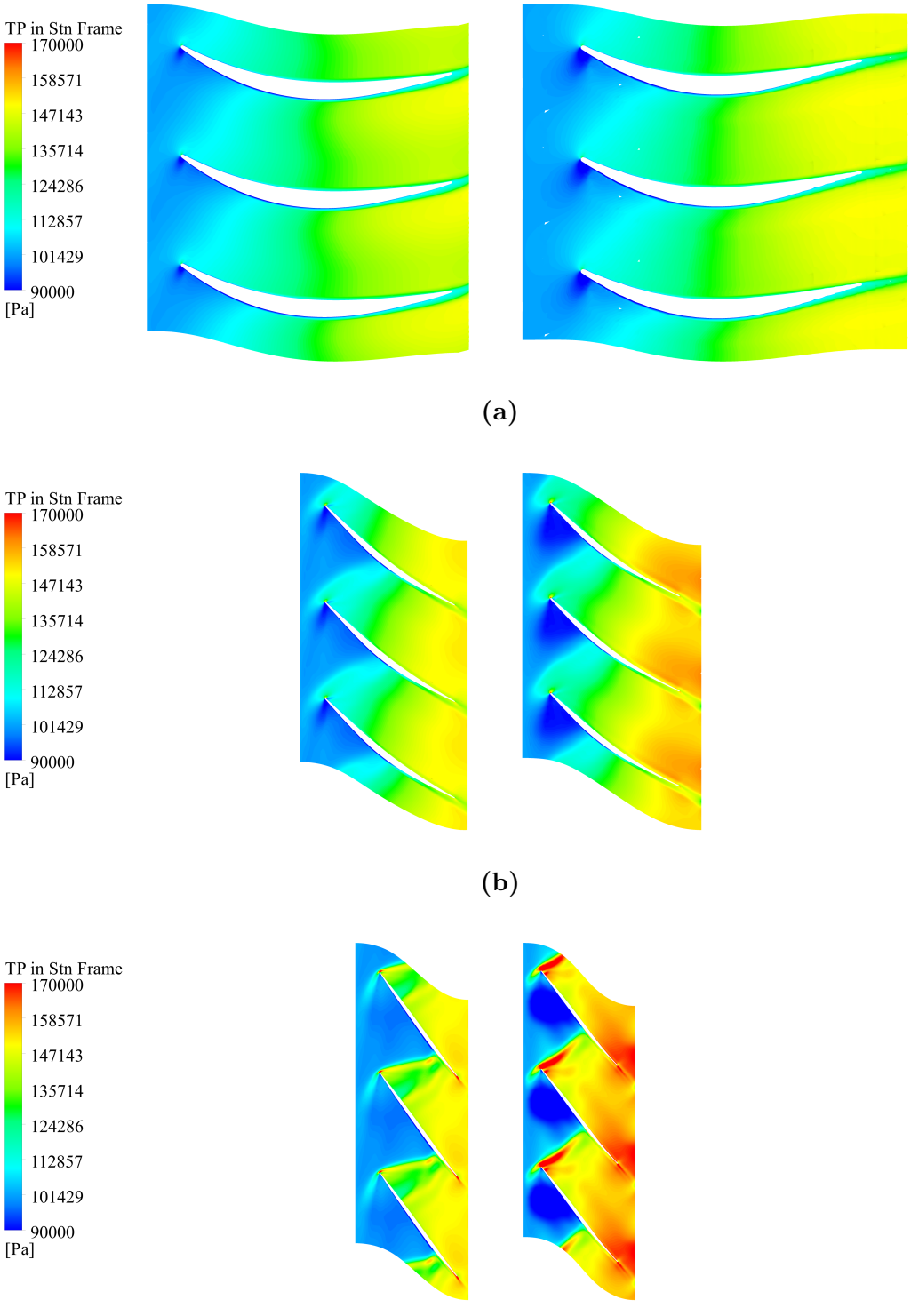

Figure 3.6: *Blade-to-blade view. CFD contours of total pressure for baseline (left) and optimized geometry (right) at span 0.1 (a), 0.5 (b) and 0.9 (c).*

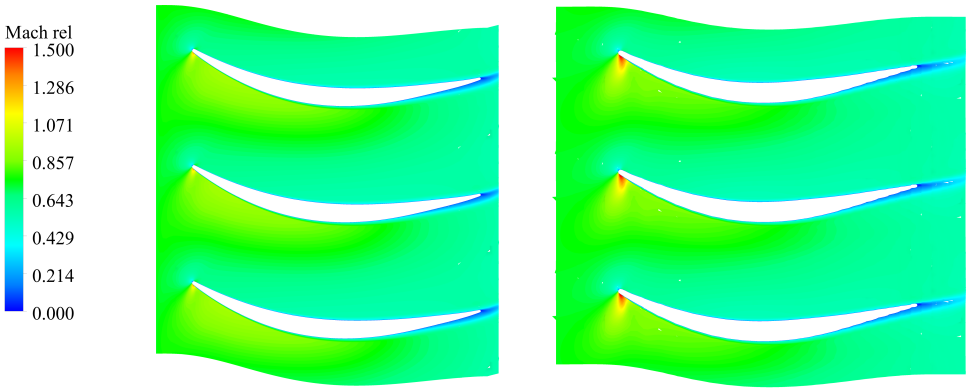

(a)

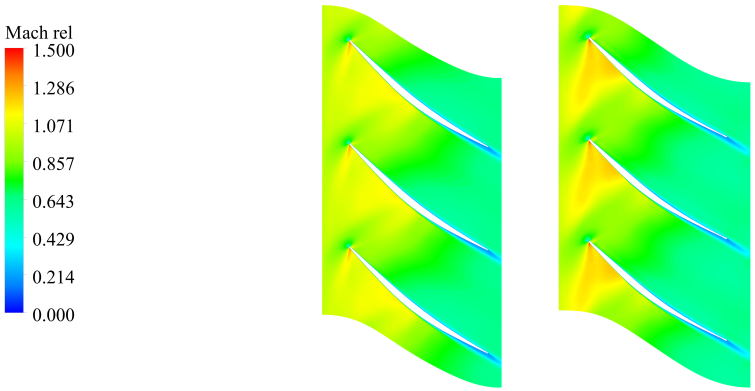

(b)

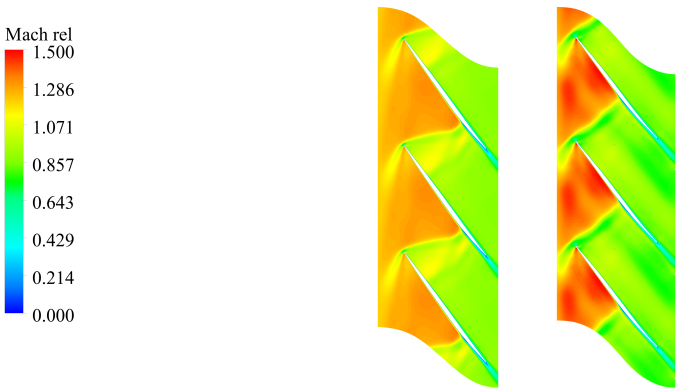

(c)

Figure 3.7: *Blade-to-blade view. CFD contours of relative Mach number for baseline (left) and optimized geometry (right) at span 0.1 (a), 0.5 (b) and 0.9 (c).*

3.3 Design under distortion conditions

As a final step, the results of the design under distorted conditions are analysed.

The optimization process is realized following the same steps as in the clean case: ML optimization, geometry reconstruction and subsequent CFD assessment. The only difference regards the inlet aerodynamic modelling, given its non-uniform nature. The distortion pattern described in subsection 2.5.2 is applied as inlet boundary condition. Therefore, the ML tool operates in distortion mode, discretizing the AIP into a user-defined number of sectors. In this thesis, the optimization through NOPTURN/SATURN is discussed, whereas the CFD assessment will be covered in future studies.

In Table 3.2 the basic settings of the optimization are reported. They are the same of ID = 2 considered in the clean design, except for the number of generations and individuals, that is reduced. Indeed, the time required in this kind of optimization is larger. The reason is that SATURN takes more time to complete a single analysis. In fact, in the sectors affected by distortion the relaxation factors are reduced to promote the convergence. The computational time required is ∼2 s in clean mode (one sector, 11 span positions) and ∼130 s in distortion mode (11 sectors, 11 span positions each), running on an Intel® Core™ i7-4510U CPU @ 2.0 GHz processor. Pareto front is shown in Figure 3.8.

The individual with maximum isentropic efficiency is chosen for the subsequent actions. The comparison between the baseline and optimized geometric variables of the rotor blade can be observed in Figure 3.9. Here, it is evident how the chord trend shows a more uniform profile than the baseline. The greatest relative differences occur for the outlet blade angle, where the optimized curve shows the maximum decrease of 10% at span 0.8. The inlet blade angle and the chord point out, respectively, less than 5.5% and 7% differences. The maximum thickness to chord ratio follows the baseline geometry.

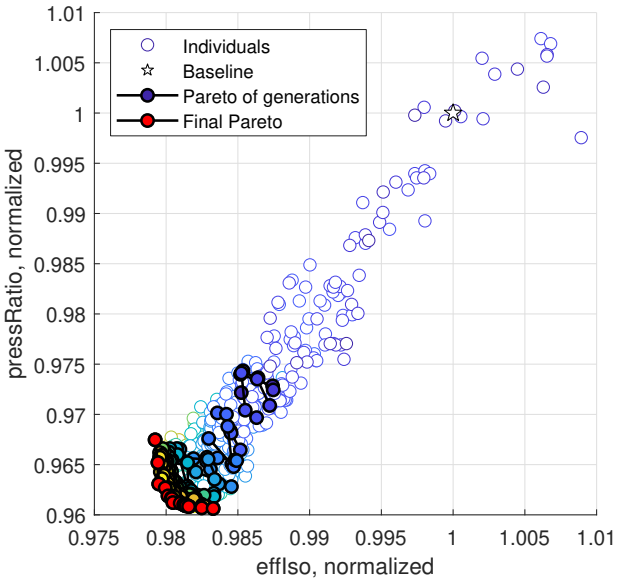

Figure 3.8: *Design under distortion conditions. Pareto front evolution.*

Optimization ID	**1**
Objectives	$\max(\eta_{iso})$ $\max(\text{TPR})$
Constraints	$\frac{\text{SM}}{\text{SM}_{base}} \geq 0.98$ $\frac{\text{CM}}{\text{CM}_{base}} \geq 0.98$
$\boldsymbol{N_r}$	11
$\boldsymbol{N_\theta}$	11
Bézier control points	5
Variables	20
Exploration range, x	15%
Exploration range, y	0%
$\boldsymbol{N_{gen}}$	30
$\boldsymbol{N_{ind}}$	45
Crossover fraction	65%
Time [s]	2.092×10^5

Table 3.2: *Optimization settings. Design under distortion conditions.*

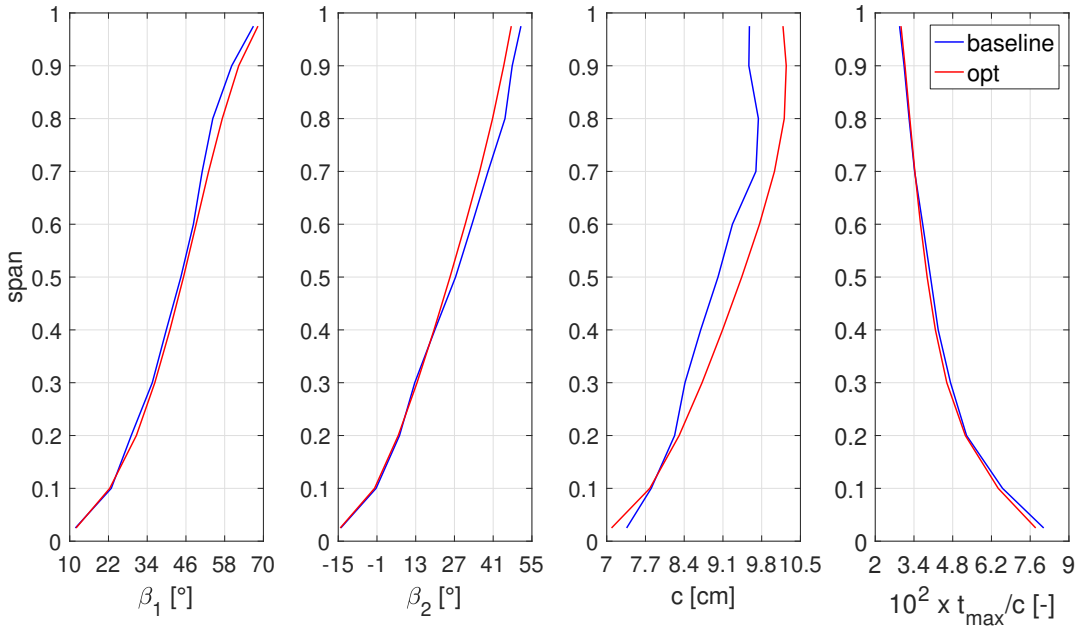

Figure 3.9: *Optimized spanwise geometry compared to baseline. From left: inlet blade angle, outlet blade angle, chord length and maximum thickness to chord ratio. Distortion case.*

3.3.1 Performance

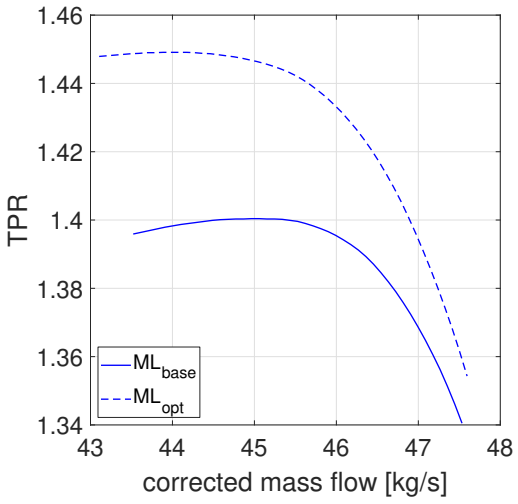

(a)

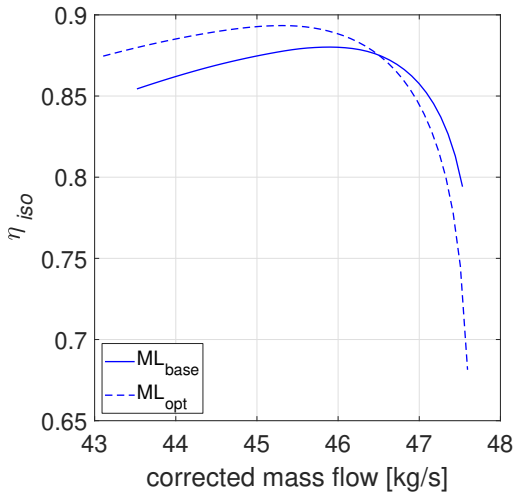

(b)

Figure 3.10: *Characteristic maps of TPR (a) and isentropic efficiency (b) under distorted conditions. ML results with R4 baseline and optimized geometry.*

The overall performance and spanwise results are reported in Figure 3.10 and Figure 3.11 respectively. They include ML outputs under distorted conditions with baseline and optimized blade profiles.

The first two plots are analysed. The optimized curves slightly shift to lower mass flow values. The exception is the unchanged choking point position, but, as said, the fine prediction of the choking condition is out of the scopes of the ML code. The prediction of surge point is seeked instead. The new geometry shows an increase of 3.36% for TPR and 1.51% for isentropic efficiency, near peak efficiency. The performance at surge point is better, with a 3.72% rise of TPR and 2.36% rise of isentropic efficiency. Meanwhile, beyond the near-peak efficiency point, the

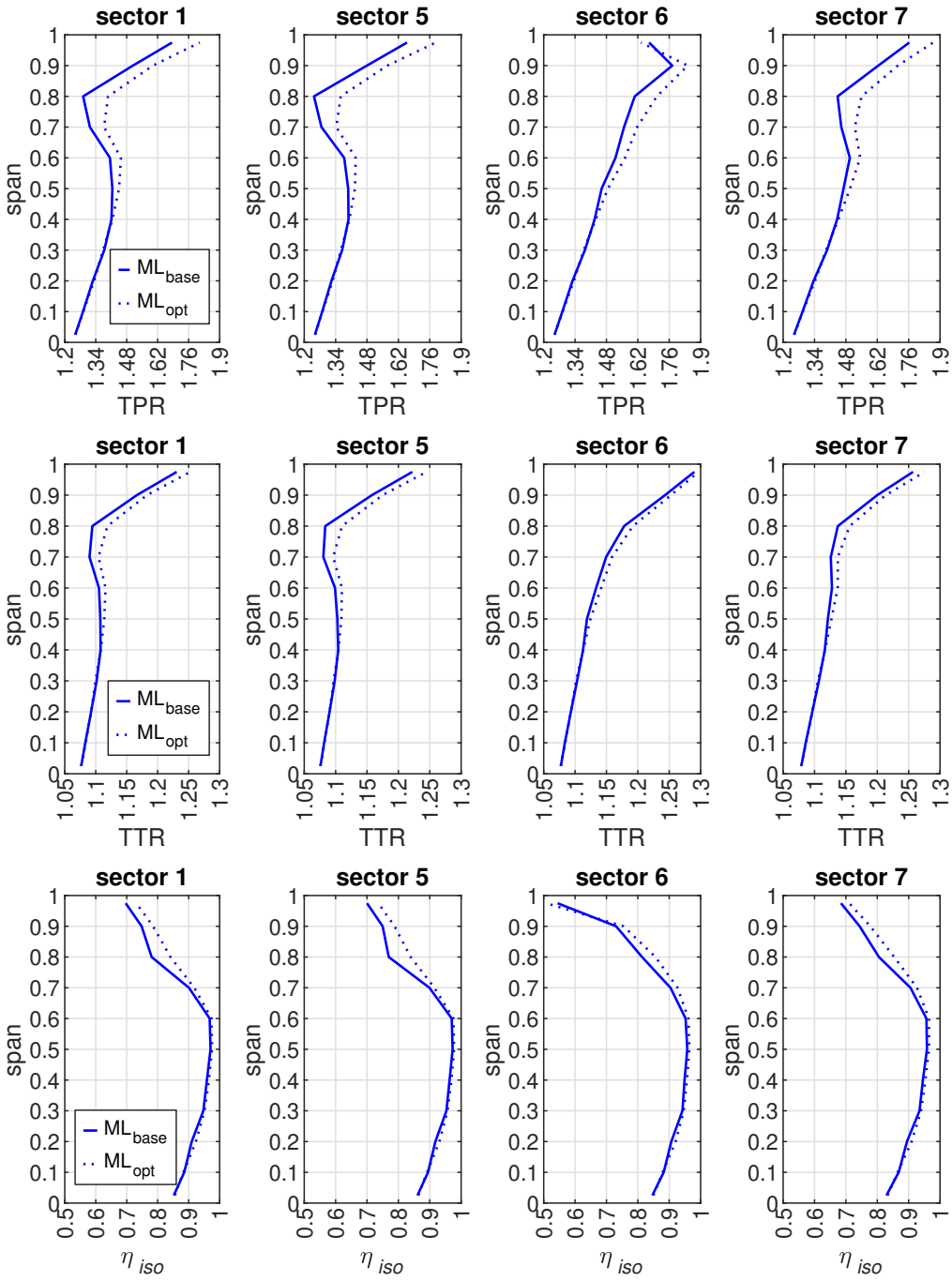

Figure 3.11: *Baseline and optimized geometry under distortion configuration. ML spanwise profiles downstream of rotor blade relative to some DC sectors. The numbering starts from 0° and follows the θ direction of Figure 2.7a. Sector 1 belongs to a clean area, the distortion is centred within sector 6.*

optimized results tend to worsen.

The spanwise profiles are close to the baseline trends both around the distortion sector (sector 6) and on the clean region (sector 1). The differences arise above midspan, where the performance shows an increase with respect to the baseline results. The resulting maximum variations occur at span 0.8 and are: 9.65% for TPR, 2.49% for TTR and 9.07% for isentropic efficiency. These values should be verified through full-annulus CFD results in a future work.

Chapter 4

Conclusions

In the present thesis, a methodology for the preliminary analysis and design of axial rotors operating under clean and distortion inflow conditions has been discussed. The numerical study is performed by 1D ML calculations, extended to a quasi-2D field through the DC approach employed for non-uniform incoming flow and coupled with a GA optimizer. The resultant predictions are then validated by means of high-order CFD approach, given that experimental results are only available for analysis under clean conditions. Single-passage simulations are carried out for the clean case, whereas full-annulus domain will be used to complete CFD assessment in the distorted case. Since a preliminary study is conducted and the investigation of the integral performance is the main purpose, steady RANS simulations are considered to create reference results for the ML approach.

The major conclusions can be drawn as follows:

- At the beginning, the validation of ML peformance with R4 baseline geometry under uniform conditions is investigated. The experimental characteristic maps are available for all the speedlines and show a good match with the low-order tool, in particular at design point;

- The second analysis involves a distortion pattern at AIP enclosed in a wedge of nearly 60°. A good comparison with CFD under distortion is exhibited around peak efficiency point. Here, the discretized ML solver shows a relative error of 0.3% for TPR and 0.6% for isentropic efficiency, even if the mass flows are slightly shifted. A weaker matching occurs at the extremities. Generally the spanwise profiles are quite close below midspan and tend to differ towards tip;

- The performance yielded by the optimized geometry under uniform conditions shows some ML limitations. Both methods present an increased TPR than the baseline geometry and a quite close peak efficiency value, although with a non-coincident mass flow. However, ML tool overpredicts the results and the surge point arises at a much lower mass flow, as opposed to the choking position. The spanwise results match at midspan, while differ towards hub and tip;

- The design optimization under distorted conditions with the ML approach needs to be weighted through CFD as future step. However, the expected rises in TPR and isentropic efficiency are met. The performance increases along span as well, most of all above midspan.

Based on these findings, the leaner low-order model shows its eligibility for design space exploration and preliminary design optimization, also due to the low computational cost and need for few geometric data. However, the extent of the discrepancies presented suggests the need for alternative correlations or calibration approaches. Moreover, better results in the preliminary design could be achieved through the implementation of an iterative procedure based on CFD results or even through the replacement of the loss models with an artificial neural network trained on RANS results. Surely, the next step will be the CFD assessment of the design under distorted conditions.

Bibliography

[1] D. S. Lee, D. W. Fahey, P. M. Forster, P. J. Newton, R. C.N. Wit, L. L. Lim, B. Owen, and R. Sausen. "Aviation and global climate change in the 21st century." *Atmospheric Environment*, Vol. 43, No. 22, pp. 3520–3537, 2009.

[2] O. Dessens, M. O. Köhler, H. L. Rogers, R. L. Jones, and J. A. Pyle. "Aviation and climate change." *Transport Policy*, Vol. 34, pp. 14–20, 2014. Air Transportation and the Environment.

[3] H. Preston, D. S. Lee, and P. D. Hooper. "The inclusion of the aviation sector within the European Union's Emissions Trading Scheme: What are the prospects for a more sustainable aviation industry?" *Environmental Development*, Vol. 2, pp. 48–56, 2012. Sustainable futures: Multi-disciplinary perspectives on multi-level transitions.

[4] "Full Forecast Document and Tables - FAA Aerospace Forecast FY 2014-2034." `https://www.faa.gov/data_research/aviation/aerospace_forecasts/media/2014_faa_aerospace_forecast.pdf`. (Accessed on 01/10/2021).

[5] J. Overton. "The Growth in Greenhouse Gas Emissions from Commercial Aviation." `https://www.eesi.org/files/FactSheet_Climate_Impacts_Aviation_1019.pdf`, October 2019. (Accessed on 01/11/2021).

[6] A. Uranga, M. Drela, E. M. Greitzer, D. K. Hall, N. A. Titchener, M. K. Lieu, N. M. Siu, C. Casses, A. C. Huang, G. M. Gatlin, et al. "Boundary Layer Ingestion Benefit of the D8 Transport Aircraft." *AIAA Journal*, Vol. 55, No. 11, pp. 3693–3708, 2017.

[7] A. Seitz, F. Peter, J. Bijewitz, A. Habermann, Z. Goraj, M. Kowalski, A. C. Pardo, C. Hall, F. Meller, R. Merkler, et al. "Concept validation study for fuselage wake-filling propulsion integration." In *31st Congress of the International Council of the Aeronautical Sciences*, pp. 09–14, 2018.

[8] A. Uranga, M. Drela, E. Greitzer, N. Titchener, M. Lieu, N. Siu, A. Huang, G. M. Gatlin, and J. Hannon. "Preliminary Experimental Assessment of the Boundary Layer Ingestion Benefit for the D8 Aircraft." In *52nd Aerospace Sciences Meeting*, 0906, 2014.

[9] J. L. Felder, G. V. Brown, H. DaeKim, and J. Chu. "Turboelectric Distributed Propulsion in a Hybrid Wing Body Aircraft." 2011.

[10] L. Menegozzo and E. Benini. "Boundary Layer Ingestion Propulsion: A Review on Numerical Modeling." *Journal of Engineering for Gas Turbines and Power*, Vol. 142, No. 12, 2020.

[11] M. Drela. "Power Balance in Aerodynamic Flows." *AIAA journal*, Vol. 47, No. 7, pp. 1761–1771, 2009.

[12] B. J. Lee, M. F. Liou, and M. S. Liou. "Conceptual Aerodynamic Design of a Tail-Cone Thruster System Under Axi-Symmetric Inlet Distortion." In *ASME Turbo*

Expo 2018: Turbomachinery Technical Conference and Exposition. American Society of Mechanical Engineers Digital Collection, 2018.

[13] E. Valencia, V. Alulema, D. Rodriguez, P. Laskaridis, and I. Roumeliotis. "Novel fan configuration for distributed propulsion systems with boundary layer ingestion on an hybrid wing body airframe." *Thermal Science and Engineering Progress*, Vol. 18, 100515, 2020.

[14] W. Thollet, G. Dufour, X. Carbonneau, and F. Blanc. "Body force modeling for aerodynamic analysis of air intake–fan interactions." *International Journal of Numerical Methods for Heat & Fluid Flow*, 2016.

[15] E. Benichou, G. Dufour, Y. Bousquet, N. Binder, A. Ortolan, and X. Carbonneau. "Body Force Modeling of the Aerodynamics of a Low-Speed Fan under Distorted Inflow." *International Journal of Turbomachinery, Propulsion and Power*, Vol. 4, No. 3, 29, 2019.

[16] Y. Ma, J. Cui, N. R. Vadlamani, and P. Tucker. "A Mixed-Fidelity Numerical Study for Fan–Distortion Interaction." *Journal of Turbomachinery*, Vol. 140, No. 9, 2018.

[17] E. J. Gunn and C. A. Hall. "Aerodynamics of Boundary Layer Ingesting Fans." In *ASME turbo expo 2014: turbine technical conference and exposition*. American Society of Mechanical Engineers Digital Collection, 2014.

[18] W. Zhang, S. Stapelfeldt, and M. Vahdati. "Influence of the inlet distortion on fan stall margin at different rotational speeds." *Aerospace Science and Technology*, Vol. 98, 105668, 2020.

[19] V. J. Fidalgo, C. A. Hall, and Y. Colin. "A Study of Fan-Distortion Interaction Within the NASA Rotor 67 Transonic Stage." *Journal of Turbomachinery*, Vol. 134, No. 5, 2012.

[20] J. J. Adamczyk. "A Model Equation for Simulating Flows in Multistage Turbomachinery." ASME Paper 85-GT-226, 1985.

[21] W. T. Cousins and M. W. Davis Jr. "Evaluating Complex Inlet Distortion With a Parallel Compressor Model: Part 1—Concepts, Theory, Extensions, and Limitations." In *Turbo Expo: Power for Land, Sea, and Air*, Vol. 54617, pp. 1–12, 2011.

[22] L. Da, L. Hanan, Y. Zhe, P. Tianyu, D. Hai, and L. Qiushi. "Optimization of a transonic axial-flow compressor under inlet total pressure distortion to enhance aerodynamic performance." *Engineering Applications of Computational Fluid Mechanics*, Vol. 14, No. 1, pp. 1002–1022, 2020.

[23] E. Valencia, V. Hidalgo, D. Nalianda, P. Laskaridis, and R. Singh. "Discretized Miller approach to assess effects on boundary layer ingestion induced distortion." *Chinese Journal of Aeronautics*, Vol. 30, No. 1, pp. 235–248, 2017.

[24] L. Menegozzo. "Development of a Numerical Code for Analysis and Design of Axial Compressors operating under Inlet Flow Distortion." PhD Thesis, Università degli Studi di Padova, 2020.

[25] X. Zheng and H. Yang. "End-Wall Boundary Layers and Blockages of Multistage Axial Compressors Under Different Conditions." *Journal of Propulsion and Power*, Vol. 33, No. 4, pp. 908–916, 2017.

[26] L. H. Smith. "Casing Boundary Layers in Multistage Axial Compressors." *Flow Research on Blading*, 1970.

[27] I. A. Johnsen and R. O. Bullock. "Aerodynamic Design of Axial-Flow Compressors. NASA SP-36." *NASA Special Publication*, Vol. 36, 1965.

[28] M. Cetin, AS Uecer, C. Hirsch, and GK Serovy. "Application of Modified Loss and Deviation Correlations to Transonic Axial Compressors." Technical report, ADVISORY GROUP FOR AEROSPACE RESEARCH AND DEVELOPMENT NEUILLY-SUR-SEINE (FRANCE), 1987.

[29] R. H. Carmody and H. F. Creveling. "Axial Flow Compressor Computer Program for Calculating Off Design Performance/Program 4." 1968.

[30] C. C. Koch and L. H. Smith Jr. "Loss Sources and Magnitudes in Axial-Flow Compressors." 1976.

[31] G. R. Miller, G. W. Lewis Jr, and M. J. Hartmann. "Shock Losses in Transonic Compressor Blade Rows." 1961.

[32] C. C. Koch. "Stalling Pressure Rise Capability of Axial Flow Compressor Stages." 1981.

[33] M. W. Benner, SA Sjolander, and SH Moustapha. "An Empirical Prediction Method for Secondary Losses in Turbines—Part I: A New Loss Breakdown Scheme and Penetration Depth Correlation." 2006.

[34] J. M. Tournier and M. S. El-Genk. "Axial Flow, Multi-Stage Turbine and Compressor Models." *Energy Conversion and Management*, Vol. 51, No. 1, pp. 16–29, 2010.

[35] M. I. Yaras and SA Sjolander. "Prediction of Tip-Leakage Losses in Axial Turbines." In *ASME 1990 International Gas Turbine and Aeroengine Congress and Exposition*. American Society of Mechanical Engineers Digital Collection, 1990.

[36] N. M. White, A. Tourlidakis, and R. L. Elder. "Axial Compressor Performance Modelling with a Quasi-one-dimensional Approach." *Proceedings of the Institution of Mechanical Engineers, Part A: Journal of Power and Energy*, Vol. 216, No. 2, pp. 181–193, 2002.

[37] I. J. Day, E. M. Greitzer, and NA Cumpsty. "Prediction of Compressor Performance in Rotating Stall." 1978.

[38] D. C. Miller and D. L. Wasdell. "Off-Design Prediction of Compressor Blade Losses." *C279/87, pgs*, pp. 249–258, 1987.

[39] C. Hughes. "Aerodynamic Performance of Scale-Model Turbofan Outlet Guide Vanes Designed for Low Noise." In *40th AIAA Aerospace Sciences Meeting & Exhibit*, 374, 2002.

[40] A. Magrini. "Study of Body Force Modeling for Coupled Fan-Intake Simulations." PhD Thesis, Università degli Studi di Padova, 2020.

[41] J. D. Anderson. "Fundamentals of Aerodynamics." 5th Edition, New York, McGraw-Hill Education, 2011, pp. 187–193.

[42] C. Favaron. "Full-Annulus Analysis of a Transonic Fan Stage under Inlet Distortions." MS Thesis, Aerospace Engineering, Università degli Studi di Padova, Padova, IT, October 2020.

[43] K. Atashkari, N. Nariman-Zadeh, N. Pilechi, A. Jamali, X. Yao. "Thermodynamic Pareto optimization of turbojet engines using multi-objective genetic algorithms." *International Journal of Thermal Sciences*, Vol. 44, No. 11, pp. 1061–1071, 2005.

[44] K. Deb. "Multiobjective Optimization Using Evolutionary Algorithms." New York, Jan., 2001.

[45] A. Konak, D. W. Coit, and A. E. Smith. "Multi-objective optimization using genetic algorithms: A tutorial." *Reliability engineering & system safety*, Vol. 91, No. 9, pp. 992–1007, 2006.

[46] N. Zanoni. "Aerodynamic Multi-Objective Optimization of a Transonic Compressor Rotor using Meanline Methods and CFD." MS Thesis, Aerospace Engineering, Università degli Studi di Padova, Padova, IT, March 2020.

[47] A. Magrini, C. Favaron, A. Visentin, L. Menegozzo, and E. Benini. "Inlet Distortion Simulations of a Transonic Fan with CFD and Low-Order Methods." In *ASME Turbo Expo 2021: Turbomachinery Technical Conference and Exposition*, Paper GT2021-58668, June 2021.

[48] L. Menegozzo, N. Zanoni, G. M. Bolla, A. Magrini, A. Visentin, and E. Benini. "Axial Rotor Design under Clean and Distortion Conditions using Mean-Line and CFD Methods." In *AIAA Scitech 2021 Forum*, 0264, 2021.